Forward–backward asymmetry in Drell–Yan muon pair production in pp collisions at $\sqrt{s} = 13$ TeV

von
Simon Hauser

BACHELORARBEIT IM FACH PHYSIK

vorgelegt der
Fakultät für Mathematik, Informatik und Naturwissenschaften der
RWTH Aachen University

im August 2018

---

angefertigt am
III. Physikalischen Institut A

bei
Prof. Dr. Thomas Hebbeker

Zweitkorrektor
Prof. Dr. Christopher Wiebusch

Kurzfassung

Diese Arbeit bestimmt die beim Drell-Yan-Prozess auftretende vorwärts-rückwärts Asymmetrie in Form des Asymmetrie-Parameters A_{fb}. Dabei werden die CMS-Daten aus dem Jahr 2016 verwendet und Myonpaare betrachtet. A_{fb} wird für die gemessenen Daten als Funktion der invarianten Masse der Myonpaare dargestellt, das Ergebnis wird mit der A_{fb}-Verteilung von Standardmodell-Simulationen verglichen. Es werden keine Abweichungen von den Vorhersagen des Standardmodells beobachtet. Desweiteren wird die A_{fb}-Verteilung unter Berücksichtigung des im ADD-Modell vorhergesagten virtuellen Graviton-Austauschs simuliert. Der Vergleich zwischen dem simulierten Signal und der Standardmodell-Simulation deutet darauf hin, dass die A_{fb}-Verteilung für Untersuchungen zur Gültigkeit des ADD-Modells geeignet ist.

Abstract

In this thesis, the Drell–Yan forward-backward asymmetry parameter A_{fb} is determined. The results of the 2016 data taking period with the CMS detector are utilized considering muon pairs. The A_{fb} parameter for the measurement as a function of the dimuon invariant mass is compared to the distribution of standard model simulations. No significant deviations from the standard model prediction are observed. Furthermore, the A_{fb} distribution is simulated also considering virtual graviton exchange predicted by the ADD model of large extra dimensions. There are clear indications for the potential of A_{fb} to distinguish between SM and virtual graviton exchange contributions.

Contents

1 Theory

1.1 The Standard Model of Particle Physics

The standard model (SM) unifies the description of three fundamental forces, electromagnetism, the weak interaction and the strong force. Gravity, the fourth fundamental force, is not yet included because all approaches to formulate a quantum field theory of gravity made so far (e.g. asymptotic safety [1]) were not renormalizable. The SM is also able to classify all known elementary particles.

While the SM has proven to be very successful in describing the wide range of processes between elementary particles [2] there are also several open questions in addition to the description of gravity as a quantum field theory. To name just a few, the mass of neutrinos [3], the existence and behaviour of dark matter [4] and dark energy [5] and the matter-antimatter asymmetry [6] is not explained by the SM. Moreover, some features of the SM are not well understood and leave room for further theoretical research, such as free parameters the SM depends on that can only be determined by experiment so far. Furthermore, the SM is not able to explain the different coupling "strength" of the fundamental forces (hierarchy problem) [7]. The following sections and paragraphs will give a short overview of selected concepts that are important for this thesis.

Fermions and Bosons

The SM particles are divided into two categories, either following Fermi-Dirac statistics or Bose-Einstein statistics. They are defined as fermions and bosons, with half-integer spin and integer spin, respectively. The elementary particles among the fermions are further subdivided into leptons and quarks. While leptons are defined as fermions which do not interact via the strong force, quarks also participate in the strong interaction.

The elementary particles among the bosons can be divided into scalar and vector bosons with spin zero and spin one, respectively. Gauge bosons are vector bosons that mediate one of the fundamental forces. The photon carries the electromagnetic force, the mediators of the strong interaction are called gluons, and the Z and W bosons carry the weak force. The hypothetical graviton mediates the force of gravity. It is also a gauge boson but has spin two and is therefore a tensor boson. In addition to that, there is a scalar boson: the Higgs boson. It is associated to the Higgs field and the Higgs mechanism that is essential to describe the mass of particles in the SM. Figure 1.1 gives an overview of the SM elementary particles.

Charges of the Standard Model

Each fundamental interaction described by the SM has an associated charge. Particles with an electromagnetic charge participate in the electromagnetic interaction, particles with color charge can interact via the strong force, and particles with weak isospin par-

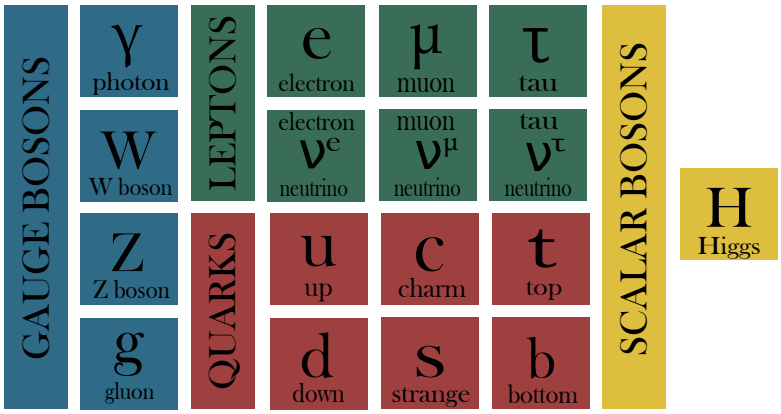

Figure 1.1: Elementary particles of the standard model.

ticipate in the weak interaction.

Leptons are either massive and carry an electromagnetic charge of $-e$, where e denotes the elementary charge, or massless and neutral, then they are called neutrinos. Quarks can be divided into up- and down-type quarks with an electromagnetic charge of $^2/_3 \cdot e$ and $^{-1}/_3 \cdot e$, respectively. All quarks have color charge that is either red, green or blue. Due to color confinement there are no free quarks observed, they form baryons (qqq), mesons ($q\overline{q}$) and other more exotic structures such as pentaquarks ($qqqq\overline{q}$) [8] instead.

While the photon, the Z boson and the Higgs boson are neutral and do not have color charge, W bosons have an electromagnetic charge of $\pm e$ and gluons have color charge. Therefore gluons can interact with each other via the strong force.
All known particles have antiparticles as their corresponding partners. Their description differs only in the sign of all additive quantum numbers, if they are all zero, particles can be their own antiparticles. In the SM, this applies for example for the photon, the Z boson and neutrinos.

1.2 Drell–Yan Process

The Drell–Yan process [9] describes the annihilation of a quark and an antiquark in hadron-hadron collisions, forming a virtual photon γ^* or Z boson and decaying into two leptons with opposite charge ($q\overline{q} \rightarrow \gamma^*/Z \rightarrow \ell^+\ell^-$). Because there are no free quarks observed the Drell–Yan process occurs in hadron-hadron collisions, for example in proton-proton collisions. Protons are not only composed of their three valence quarks, two up quarks and one down quark. They also consist of virtual quark-antiquark pairs called sea quarks. In hadron-hadron collisions involving both sea quarks and valence quarks, such as the Drell–Yan process, the sea quarks carry less momentum than the

valence quarks in general. Figure 1.2 shows the Feynman diagram for the Drell–Yan process at tree level.

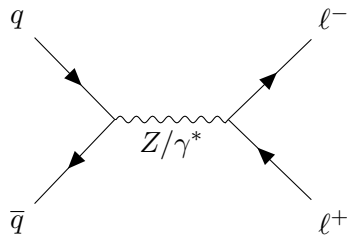

Figure 1.2: Feynman diagram for the Drell–Yan-Process.

Unless otherwise stated, the time axis in Feynman diagrams runs from left to right, while the orientation of the arrows relative to the time axis defines particles and antiparticles. In addition to that it is also distinguished between particles and antiparticles in the labels. The general structure of the differential cross section for the Drell–Yan process at next-to-leading order is given by [10]

$$\begin{aligned}\frac{d^2\sigma}{d\cos\theta_l d\phi_l} \propto [&(1+\cos^2(\theta_l)) + A_0\frac{1}{2}(1-3\cos^2(\theta_l)) \\ &+ A_1\sin(2\theta_l)\cos(\phi_l) + A_2\frac{1}{2}\sin^2(\theta_l)\cos(2\phi_l) \\ &+ A_3\sin(\theta_l)\cos(\phi_l) + A_4\cos(\theta_l) + A_5\sin^2(\theta_l)\sin(2\phi_l) \\ &+ A_6\sin(2\theta_l)\sin(\phi_l) + A_7\sin(\theta_l)\sin(\phi_l)].\end{aligned} \tag{1.1}$$

The angle of the negatively charged lepton relative to the direction of the incoming quark in the dilepton rest frame is denoted by θ_ℓ, while ϕ_l is the associated azimuthal angle. The coefficients A_i depend on the interaction scale, the electroweak mixing angle θ_W (Weinberg angle), the weak isospin and the electromagnetic charges of the participating fermions. At leading order, the differential cross section can be expressed as [11]

$$\frac{d\sigma}{dy} = C\left[\frac{3}{8}(1+y^2) + A_{\mathrm{fb}}\cdot y\right], \tag{1.2}$$

where $y = \cos(\theta_l)$. After defining forward events by $y > 0$ and backward events by $y < 0$, one can see from equation 1.2 that there is a forward-backward asymmetry, caused by the linear term in y and therefore dependent on the asymmetry parameter A_{fb}. In the next section the asymmetry will be further discussed based on the differential cross section at leading order.

1.3 Drell–Yan angular Forward-Backward Asymmetry

The reason for the occurrence of the Drell–Yan forward-backward asymmetry is the fact that the gauge bosons of the electroweak interaction show axial vector coupling and

vector coupling to fermions as well. To obtain the commonly used definition of the asymmetry parameter starting from equation 1.2 the total forward cross section is introduced:

$$\sigma_{\mathrm{f}} = \int_0^1 \frac{d\sigma}{dy} dy = \frac{C}{2}\Big(1 + A_{\mathrm{fb}}\Big). \tag{1.3}$$

Similarly, one derives the backward total cross section:

$$\sigma_{\mathrm{b}} = \int_{-1}^0 \frac{d\sigma}{dy} dy = \frac{C}{2}\Big(1 - A_{\mathrm{fb}}\Big). \tag{1.4}$$

Based on equations 1.3 and 1.4 the asymmetry parameter A_{fb} is defined as

$$A_{\mathrm{fb}} = \frac{\sigma_{\mathrm{f}} - \sigma_{\mathrm{b}}}{\sigma_{\mathrm{f}} + \sigma_{\mathrm{b}}}. \tag{1.5}$$

As a function of the dilepton invariant mass, its numerical value is expected to be less than zero below the Z boson mass peak, where the interaction is dominated by the exchange of virtual photons and close to zero in the Z peak region, because the vector coupling of leptons to Z bosons is small. Furthermore, A_{fb} is expected to be positive for dilepton invariant masses above the Z peak as the values for the asymmetry parameter are determined by virtual photon and Z interference [12].

It is important to note that the definition of A_{fb} given in equation 1.5 and the definition used for the determination of A_{fb} in this thesis are not exactly the same. While θ_ℓ is the angle of the negatively charged lepton relative to the incoming quark in the dilepton rest frame, this thesis uses the polar angle θ_{CS} in the Collins–Soper frame that is defined in section 1.4. Therefore, forward and backward events are defined via $\cos(\theta_{\mathrm{CS}}) > 0$ and $\cos(\theta_{\mathrm{CS}}) < 0$, respectively. It is reasonable to utilize $\theta_{\mathrm{CS}} = \theta_l$ as an approximation [13]. In the following, a brief overview of the relation between the vector and axial vector couplings of the photon and the Z boson and A_{fb} is given using the angle θ_ℓ. This overwiew is based on the references [12], [14] and [15].

The left-handed and right-handed couplings are related to the vector and axial vector couplings via $C_L = C_V - C_A$ and $C_R = C_V + C_A$. Table 1.1 on the next page gives an overview of the left-handed and right-handed couplings of the photon and the Z boson to first generation quarks and muons. For the sake of clarity, the quantities g_z and ϑ are introduced with

$${g_z}^2 = \frac{e^2}{\vartheta(1-\vartheta)} \quad \text{and} \quad \vartheta = \sin^2(\theta_W). \tag{1.6}$$

The elementary charge is denoted by e. To deduce the connection between A_{fb} and the left-handed and right-handed couplings, the scattering amplitudes are expressed as:

$$A_{ij} = A(q_j\overline{q} \to \mu_k^-\mu^+) = -Qe^2 + \frac{\hat{s}}{\hat{s} - {M_Z}^2 + iM_Z\Gamma_Z} {C_j}^Z(q){C_k}^Z(\mu^-). \tag{1.7}$$

Here, Q denotes the charge of the respective quark in multiples of the elementary charge, $\hat{s}$ is the parton interaction scale and M_Z is the mass of the Z boson. Γ_Z denotes the decay width of the Z boson.

Table 1.1: Left-handed and right-handed couplings of the Z boson and the photon to first generation quarks and muons.

	$C_{L/R}$	γ	Z
up quark	C_L	$2e/3$	$g_z\left(-\frac{1}{2}+\frac{2}{3}\vartheta\right)$
	C_R	$2e/3$	$g_z\left(\frac{2}{3}\vartheta\right)$
down quark	C_L	$-e/3$	$g_z\left(\frac{1}{2}-\frac{1}{3}\vartheta\right)$
	C_R	$-e/3$	$g_z\left(-\frac{1}{3}\vartheta\right)$
Muon	C_L	$-e$	$g_z\left(\frac{1}{2}-\vartheta\right)$
	C_R	$-e$	$g_z\left(-\vartheta\right)$

The differential cross section can then be expressed in terms of the scattering amplitudes, yielding

$$\frac{d\sigma}{dy} = \frac{1}{128\pi\hat{s}}\left[\left(|A_{LL}|^2+|A_{RR}|^2\right)(1+y)^2+\left(|A_{LR}|^2+|A_{RL}|^2\right)(1-y)^2\right]. \tag{1.8}$$

As done in the equations 1.3 and 1.4, the total forward cross section and the total backward cross section are obtained via integrating the differential one for $0 < y < 1$ and $-1 < y < 0$, respectively.

$$\sigma_\mathrm{f} = \int_0^1 \frac{d\sigma}{dy}dy = \frac{1}{128\pi\hat{s}}\left[\frac{7}{3}\left(|A_{LL}|^2+|A_{RR}|^2\right)+\frac{1}{3}\left(|A_{LR}|^2+|A_{RL}|^2\right)\right] \tag{1.9}$$

$$\sigma_\mathrm{b} = \int_{-1}^0 \frac{d\sigma}{dy}dy = \frac{1}{128\pi\hat{s}}\left[\frac{1}{3}\left(|A_{LL}|^2+|A_{RR}|^2\right)+\frac{7}{3}\left(|A_{LR}|^2+|A_{RL}|^2\right)\right] \tag{1.10}$$

Inserting the equations 1.9 and 1.10 in equation 1.5 yields

$$A_\mathrm{fb} = \frac{3}{4}\frac{\left(|A_{LL}|^2+|A_{RR}|^2\right)-\left(|A_{LR}|^2+|A_{RL}|^2\right)}{\left(|A_{LL}|^2+|A_{RR}|^2\right)+\left(|A_{LR}|^2+|A_{RL}|^2\right)}. \tag{1.11}$$

The result is evaluated using measured values of the occurring quantities, an overview of them is given in table 1.2.

Table 1.2: Numerical values used for the theoretical calculation of the asymmetry parameter A_{fb}.

Quantity	Information
$e = \sqrt{4\pi\alpha}$	For the calculation $\alpha \approx \alpha_Z = 1/128$ is used, which is only a rough approach because α depends on the energy scale and α_Z corresponds to the Z boson mass peak.
$Q = \frac{2}{3}$	By using this value, an up quark is chosen for the calculation. Setting $Q = -1/3$ (down quark) does not notably change figure 1.3.
$\vartheta = \sin^2\theta_W = 0.23155$ [16]	The Weinberg angle is energy scale dependent as well, while the given value corresponds to the Z peak.
$M_Z = 91.1876\,\mathrm{GeV}$ [17]	A_{fb} in figure 1.3 has its zero near the Z boson mass.
$\Gamma_Z = 2.4952\,\mathrm{GeV}$ [17]	The full decay width is used for the calculation.

Figure 1.3 shows the resulting theoretical prediction for the asymmetry parameter A_{fb} based on equation 1.11. The shape is in line with the general expectation given at the beginning of this section: A_{fb} is predicted to be lower than zero for $\hat{s}$ below the Z boson mass peak, close to zero near the Z peak and greater than zero for higher $\hat{s}$.

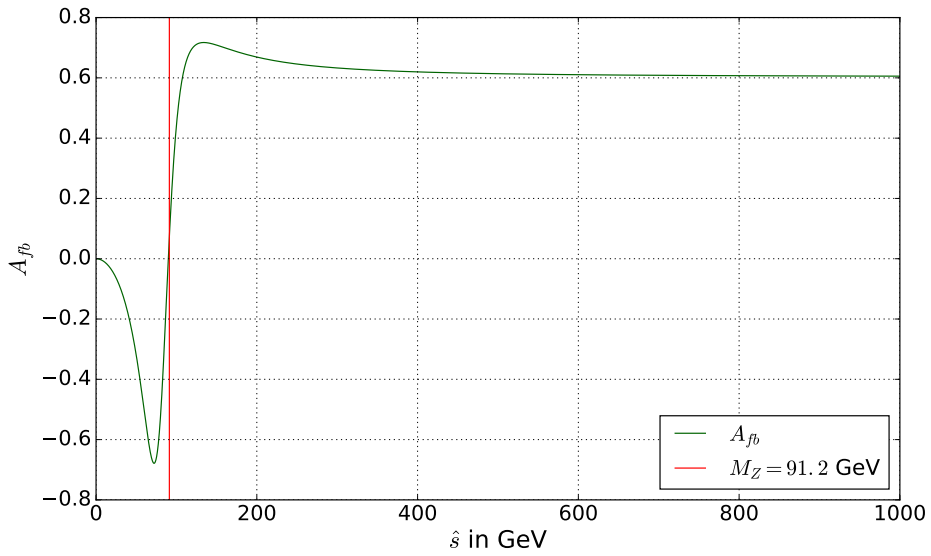

Figure 1.3: Theoretical prediction for A_{fb}.

1.4 Collins–Soper Frame

In hadron-hadron collisions the interacting quarks have transverse momentum in general which particularly holds true for the Drell–Yan process. To minimize the impact the Collins–Soper frame [18] is utilized which is defined in the rest frame of the lepton-antilepton pair. As is depicted in figure 1.4 the z-axis is defined by the line bisecting the angle 2α which is measured between the negative of the momentum vector of the incoming proton p_1 and the momentum vector of the second incoming proton p_2.

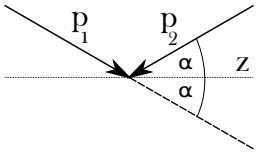

Figure 1.4: Definition of the z-axis of the Collins–Soper frame.

Figure 1.5 gives an overview of the Collins–Soper frame. The momentum vectors of the incoming protons and the produced leptons define the hadron plane and the lepton plane, respectively. The x-axis extends through the lepton plane and stands orthogonal on the z-axis, while the y-axis is chosen such that the resulting coordinate system is right handed. Furthermore, the azimuthal angle ϕ_{CS} is the smaller one of the two angles between the hadron plane and the lepton plane. The polar angle θ_{CS} is defined as the angle between the momentum vector of the negatively charged lepton and the z-axis.

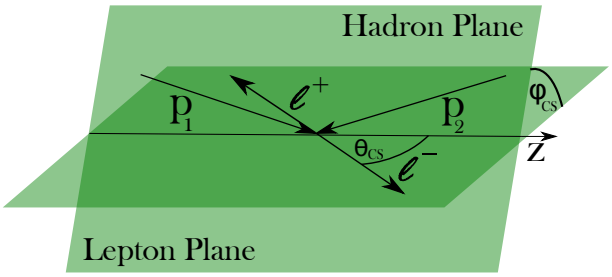

Figure 1.5: Construction of the Collins–Soper frame.

The polar angle can be determined as follows:

$$\cos(\theta_{\mathrm{CS}}) = \frac{{p_z}^{\ell\ell}}{|{p_z}^{\ell\ell}|} \cdot \frac{2({p_1}^{+}{p_2}^{-} - {p_1}^{-}{p_2}^{+})}{\sqrt{{M_{\ell\ell}}^2((M_{\ell\ell})^2 + ({p_T}^{\ell\ell})^2)}}. \tag{1.12}$$

While already depicted in figure 1.5, equation 1.12 defines the orientation of the z-axis. All relevant quantities occurring are only named in the following paragraph but are

defined and further explained in section 2.4. The dilepton invariant mass is denoted by $M_{\ell\ell}$, while ${p_{\mathrm{T}}}^{\ell\ell}$ is the transverse momentum of the dilepton system and ${p_z}^{\ell\ell}$ is the longitudinal component of the absolute value of the momentum vector. The indices "1" and "2" represent the lepton and antilepton, respectively. The quantities ${p_i}^{\pm}$ are defined via ${p_i}^{\pm} = (E_i \pm {p_i}^3)/\sqrt{2}$ where E_i denotes the energy and ${p_i}^z$ is the z component of the momentum vector.

1.5 Large Extra Dimensions

One of the numerous theories that predict physics beyond the standard model to adress the issues mentioned in section 1.1 is the ADD (Nima Arkani-Hamed, Savas Dimopoulos, Gia Dvali) model [19]. By introducing large extra dimensions (LED), the ADD model aims to provide a "natural" solution to the hierarchy problem. It assumes that only gravity can propagate through all dimensions causing its apparent "weakness" with respect to the other fundamental forces.

For this thesis it is especially important that the aforementioned gauge boson of quantum gravity, the graviton, could be produced in proton-proton collisions as a virtual particle. Furthermore, the graviton could decay into a lepton-antilepton pair [20]. Through interference with the Drell–Yan process this decay would constitute a contribution to the dilepton mass spectrum. The differential cross section for the production of gravitons via gluon-gluon fusion ($gg \to G^* \to \ell^+\ell^-$) in LO can be expressed as [21]

$$\frac{d\sigma^{\mathrm{LED}}}{dy} = C^{\mathrm{LED}} \left[(1+y^2)(1-y^2)\right] \tag{1.13}$$

where $y = \cos(\theta_\ell)$ and θ_ℓ denotes the angle of the negatively charged lepton relative to the direction of the incident quark again. C^{LED} can be parametrized as a function of the ultraviolet cutoff parameter Λ_T that cannot be calculated explicitly without the knowledge of the full quantum gravity theory. Because the dominant angular dependencies differ for the Drell–Yan process and the virtual graviton exchange in this frame, it is concluded that the A_{fb} distribution for the Drell–Yan process changes assuming virtual graviton exchange as an additional contributing process. This is further discussed in section 8.

2 The CMS experiment at the LHC at CERN

2.1 The European Organization for Nuclear Research

The European Organization for Nuclear Research (CERN) is located near Geneva in the border region of France and Switzerland. With its 22 member states [22] and an annual budget of more than one billion Swiss francs in 2017 [23] CERN is one of the largest scientific projects in the world. To explore the structure of matter and the fundamental interaction between their smallest parts it provides a network of particle accelerators and detectors which is shown in figure 2.1.

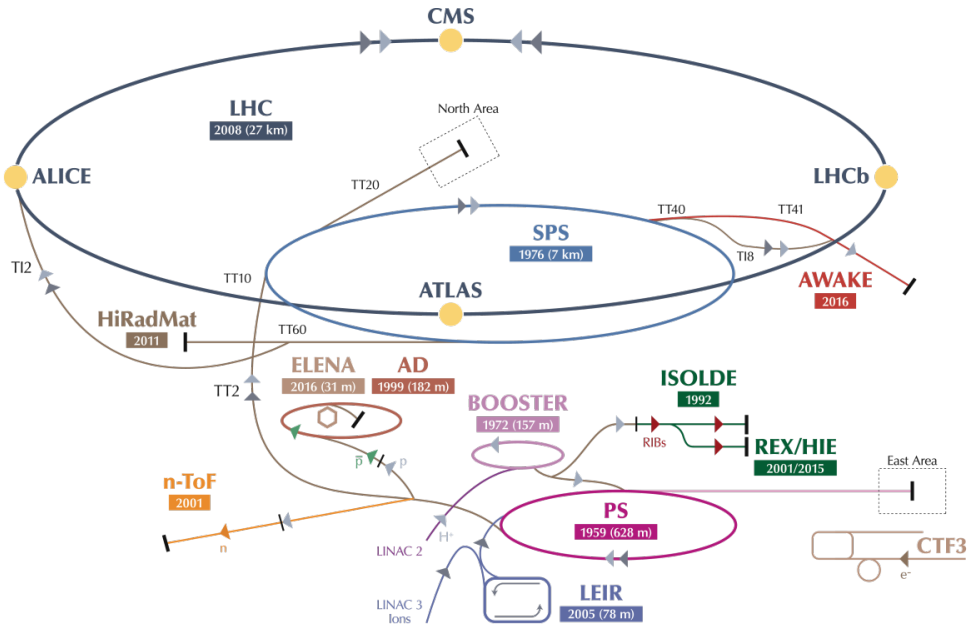

Figure 2.1: The CERN accelerator complex [24].

Using particle accelerators has proven to be a very successful way to increase the understanding of the fundamental characteristics of matter. At CERN, the vector bosons of the weak interaction, Z and $W^{\pm}$, could be detected for which Carlo Rubbia and Simon van der Meer were awarded with the Nobel Prize in 1984. The latest milestone is the discovery of the Higgs boson at the LHC [25].

Currently, there are several accelerators in operation, all of them are displayed in figure 2.1 along with their construction year and scope. LINAC 2 provides protons that are further accelerated in the Proton Synchrotron Booster (BOOSTER) then transferred to the Proton Synchrotron (PS) and later brought into the Super Proton Synchrotron (SPS). Subsequently, the particle meets the requirements to be injected into the Large Hadron Collider (LHC).

2.2 The Large Hadron Collider

With superconducting magnets generating a field of 8.3 T, a scope of 27 km and a peak power of 95 MW [26], the Large Hadron Collider (LHC) is the largest particle accelerator in the world. As a collider, the LHC consists primarily of two storage rings in which the particles circle in opposite directions. The beams collide at four intersection points, where they are strongly focused to reach a maximum amount of interactions. The collisions are measured with detectors, it is differentiated between general-purpose detectors and specialised detectors. While the former are utilized to test the SM in various ways and search for new physics beyond the SM, the latter are build to explore specific phenomena. The following table 2.1 gives a brief overview of detectors at the LHC.

Table 2.1: Detector experiments at the LHC.

Experiment	Purpose [27]
ALICE (**A** **L**arge **I**on **C**ollider **E**xperiment)	specialised for heavy ion physics (e.g. studies of quark gluon plasma)
ATLAS (**A** **T**oroidal **L**HC **A**pparatu**S**)	general-purpose detector
CMS (**C**ompact **M**uon **S**olenoid)	general-purpose detector
LHCb (**L**arge **H**adron **C**ollider **b**eauty)	focused on bottom quark physics
LHCf (**L**arge **H**adron **C**ollider **f**orward)	simulates cosmic rays
MOEDAL (**MO**nopole and **E**xotics **D**etector **A**t the **L**HC)	searches for a magnetic monopole
TOTEM (**TOT**al **E**lastic and Diffractive Cross Section **M**easurement)	characteristics of the proton at small detector angles

2.3 The Compact Muon Solenoid

As already mentioned, the Compact Muon Solenoid (CMS) detector is one of the two general-purpose detectors at the LHC. In this part, some information about the composition and functionality of the CMS given. Figure 2.2 provides an overview of the structure.

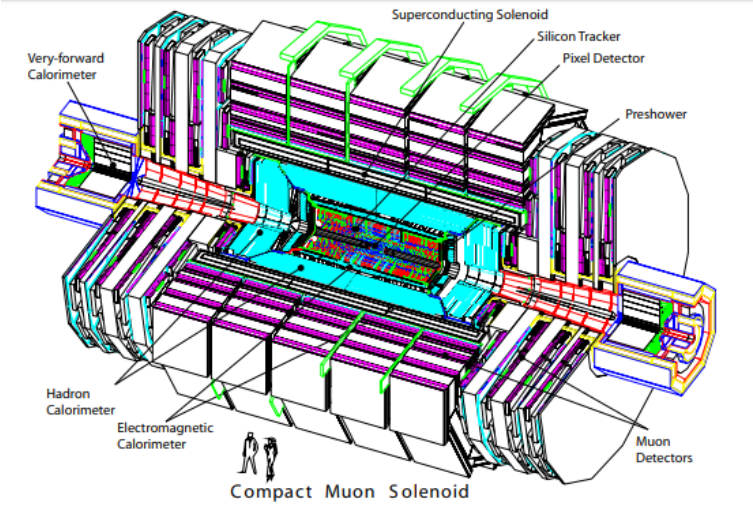

Figure 2.2: The CMS detector and its structure, concentric layers and functional components [28].

With a diameter of 6 m and a homogeneous magnetic field of 3.8 T the superconducting solenoid is one of the most substantial features of CMS. While the tracking system, the electromagnetic calorimeter and the hadronic calorimeter are situated inside, the muon system is located outside the solenoid.

When a collision takes place, the produced particles run through several detector components. In this thesis, the production of muon-antimuon pairs is studied. Therefore the functionality of the detector is described exemplary for a muon. Unless statet otherwise, the explanation follows reference [28].

After the muon is produced, it passes through the inner tracking system. The CMS tracker system consists of two parts, an inner pixel detector system with three barrel layers and an outer silicon strip tracker with another ten barrel layers. Like the whole detector, the inner tracking system has also an endcap region to cover all events up to $|\eta| < 2.5$ where η denotes the pseudorapidity that is introduced in section 2.4. Two disks for the pixel detector and another twelve for the silicon strip tracker complete the tracking system. Its main purposes are the precise measurement of the trajectory of the particle and the reconstruction of secondary vertices. Because the muon is a charged

particle its trajectory is bent in the magnetic field. Therefore, not only the sign of its charge but also the transverse momentum can be determined, although it cannot be identified unambiguously as a muon in this part of the detector.

The next outer shell is the Electromagnetic Calorimeter (ECAL). The ECAL consists of crystalline lead tungstate scintillators combined with avalanche photodiodes in the barrel region and vacuum triodes in the endcap region to transform the scintillation signals into evaluable electronic ones. Particles deposit energy in the ECAL resulting in the production of scintillation photons that can be measured by the detector components. Especially for the detection of electrons and photons the ECAL is an important procurer of information.

What the ECAL provides for example for photons and electrons is provided by the Hadronic Calorimeter (HCAL) for hadrons. It is a sampling calorimeter, therefore it consists of alternating patterns of absorber material (steel or brass) and active scintillation material (plastic). The HCAL is essential for the measurement of jets. Jets arise from the hadronization of a quark or a gluon resulting in the production of multiple hadrons and other particles.

While all layers previously described are situated inside the superconducting solenoid the next and outermost layer is located on the outside of the solenoid and of particular interest for the detection of muons. The muon system of the CMS detector has three tasks: The first one is to unequivocally identify muons, which is possible in the outer region of the detector because most other particles were stopped either by the calorimeters or by the steel of the return yoke. The second one is to measure the momentum of the muons as precisely as possible. To fulfil this goal, the barrel region of the muon system consists of four muon stations equipped with drift tube (DT) chambers and resistive plate chambers (RPC) interleaved by the flux-return yoke of the solenoidal magnet. In the two endcap regions, where the magnetic field and the expected rate is higher, the CMS detector uses cathode strip chambers (CSC) and again resistive plate chambers. The third task is to serve as a trigger. Since the amount of data produced when the LHC is running is not processable, there is a trigger system that reduces the rate in two steps via the L1 Trigger and the High-Level Trigger (HLT) from a few 100 MHz to around 600 Hz.

2.4 Important Quantities and the CMS Coordinate System

Before some important quantities of the CMS detector are introduced and explained, the CMS coordinate system is presented in this section. The z-axis points in the beam direction while the x-axis and the y-axis stand up orthogonally on z. The y-axis is oriented vertically to the storage ring plane and the x-axis points towards its center. Furthermore, the azimuthal angle ϕ is defined from the x-axis in the xy plane and the corresponding radial coordinate is denoted by r. The associated polar angle θ lies in the rz plane.

Extending from this coordinate system, several important quantities can be introduced. The transverse momentum p_{T} of a particle is defined via

$$p_{\mathrm{T}} = p \cdot \sin(\theta) \tag{2.1}$$

with the polar angle θ and the absolute value of the momentum p. Analogously, the transverse energy is calculated using

$$E_{\mathrm{T}} = E \cdot \sin(\theta) \tag{2.2}$$

where E denotes the total energy of the particle. The pseudorapidity η is defined by

$$\eta = -\ln\left(\tan\left(\frac{\theta}{2}\right)\right). \tag{2.3}$$

At colliders, it is a convention to use η instead of the polar angle θ because differences $\Delta\eta$ are Lorentz invariant under boosts along the longitudinal axis. The distance of two particles inside the detector can be calculated via

$$\Delta R = \sqrt{(\Delta\phi)^2 + (\Delta\eta)^2} \tag{2.4}$$

where $\Delta\phi$ denotes the difference of their azimuthal angles.
Another important quantity is the invariant mass of a system with two particles a and b which can be expressed as follows:

$$M_{ab} = \sqrt{(E_a + E_b)^2 - (\mathbf{p}_a + \mathbf{p}_b)^2}. \tag{2.5}$$

The energies E_a and E_b of the particles as well as their momentum vectors $\mathbf{p}_a$ and $\mathbf{p}_b$ are needed to determine its value.
In this thesis, the invariant mass of a muon-antimuon pair is used frequently. The conditions at the LHC make it necessary to consider the highly relativistic case, the dimuon invariant mass can then be calculated with the equation below utilizing several quantities defined above:

$$M_{\mu\mu} = \sqrt{2 p_{T_1} p_{T_2} \left(\cosh\left(\eta_1 - \eta_2\right) - \cos\left(\phi_1 - \phi_2\right)\right)}. \tag{2.6}$$

The properties of the muon are indexed with "1", the properties of the antimuon with "2".

3 Data Sets and Monte Carlo Samples

To perform this analysis, numerous different samples are used. Monte Carlo (MC) simulations of the Drell–Yan process and several other standard model processes that provide dimuon final states are used for the comparison with the measured data. Furthermore, the ADD model virtual graviton exchange is simulated to compare the results with the simulation of the standard model processes and the measurement. In this section, the data sets and the Drell–Yan samples are listed and the standard model background estimation is presented as well as the simulated signal samples. To analyse the samples, this thesis utilizes the software framework developed by the CMS Collaboration (CMSSW).

3.1 Data Sets

In the following section, the single muon datasets used for this thesis are presented. The analysis is performed with the results of the 2016 data-taking period, corresponding to a center-of-mass energy of $\sqrt{s} = 13\,\text{TeV}$ for the LHC proton-proton operation mode. The total integrated luminosity is displayed in table 3.1 where the datasets and their respective integrated luminosities are listed.

Table 3.1: Different single muon datasets used.

Set	$\mathcal{L}$ [fb^{-1}]
/SingleMuon/Run2016B-23Sep2016-v3/MINIAOD	5.8
/SingleMuon/Run2016C-23Sep2016-v1/MINIAOD	2.6
/SingleMuon/Run2016D-23Sep2016-v1/MINIAOD	4.3
/SingleMuon/Run2016E-23Sep2016-v1/MINIAOD	4.0
/SingleMuon/Run2016F-23Sep2016-v1/MINIAOD	3.1
/SingleMuon/Run2016G-23Sep2016-v1/MINIAOD	7.7
/SingleMuon/Run2016H-PromptReco-v2/MINIAOD	8.6
/SingleMuon/Run2016H-PromptReco-v3/MINIAOD	0.2
Total	36.3

The total integrated luminosities are calculated via pixel cluster counting (PCC). Following [29] and [30], the per-bunch instantaneous luminosity L is proportional to the number of collisions per crossing μ:

$$f \cdot \mu = \mathrm{L} \cdot \sigma_0. \tag{3.1}$$

In this equation, f denotes the rotation frequency of the bunches inside the beam pipes and σ_0 describes the total proton-proton minimum bias cross section. By defining the average number of pixel clusters per bunch crossing as $\langle N_{\text{cluster}} \rangle = \langle N_{\text{cluster/interaction}} \rangle \cdot \mu$

and the visible cross section via ${\sigma_{\text{vis}}}^{\text{PCC}} = \langle N_{\text{cluster/interaction}} \rangle \cdot \sigma_0$, one obtains

$$\text{L} = \frac{\langle N_{\text{cluster}} \rangle \cdot f}{{\sigma_{\text{vis}}}^{\text{PCC}}}. \tag{3.2}$$

The total estimated uncertainty on this calculation arises to 2.5 % [29]. Utilizing equation 3.2, the total integrated luminosity can be derived.

3.2 Drell–Yan Samples

After giving some information on the Drell–Yan process in general in section 1.2 and especially on the forward-backward angular asymmetry in section 1.3, the samples for simulating the Drell–Yan process are listed below in the tables 3.2 and 3.3. All samples included in the first table have been generated by POWHEG BOX V2 [31] in next-to-leading order (NLO) perturbative QCD and PYTHIA 8.2 [32] covering hadronization and parton showering. To simulate the parton distribution functions NNPDF 3.0 [33] was applied. The parton distribution function (PDF) set is calculated taking into account data measured with ATLAS, LHCb, HERA and CMS and other experiments. The associated cross sections were determined using FEWZ 3.1b2 [34], [35] while the electroweak interaction is considered up to NLO and corrections in perturbative QCD are applied up to next-to-next-to-leading order (NNLO).

Table 3.2: Different Drell–Yan samples used (1/2).

Number	Samples	σ [fb]	Precision
1.1	ZToMuMu_NNPDF30_13TeV-powheg_M_50_120	$1.98 \cdot 10^6$	NLO
1.2	ZToMuMu_NNPDF30_13TeV-powheg_M_120_200	$1.93 \cdot 10^4$	NLO
1.2	ZToMuMu_NNPDF30_13TeV-powheg_M_200_400	$2.73 \cdot 10^3$	NLO
1.4	ZToMuMu_NNPDF30_13TeV-powheg_M_400_800	$2.41 \cdot 10^2$	NLO
1.5	ZToMuMu_NNPDF30_13TeV-powheg_M_800_1400	$1.68 \cdot 10^1$	NLO
1.6	ZToMuMu_NNPDF30_13TeV-powheg_M_1400_2300	1.39	NLO
1.7	ZToMuMu_NNPDF30_13TeV-powheg_M_2300_3500	$8.95 \cdot 10^{-2}$	NLO
1.8	ZToMuMu_NNPDF30_13TeV-powheg_M_3500_4500	$4.14 \cdot 10^{-3}$	NLO
1.9	ZToMuMu_NNPDF30_13TeV-powheg_M_4500_6000	$4.56 \cdot 10^{-4}$	NLO
1.10	ZToMuMu_NNPDF30_13TeV-powheg_M_6000_Inf	$2.06 \cdot 10^{-5}$	NLO

For the second part the samples were provided by Markus Radziej [36]. They are generated using PYTHIA 8.2 and a PDF set calculated with NNPDF 2.3 in leading order (LO) perturbative QCD. The corresponding cross sections are determined using PYTHIA 8.2 as well.

Table 3.3: Different Drell–Yan samples used (2/2).

Number	Samples	σ [fb]	Precision
2.1	ZToMuMu_NNPDF23_13TeV-pythia_M_300_13000	$1.68 \cdot 10^3$	LO
2.2	ZToMuMu_NNPDF23_13TeV-pythia_M_500_13000	$2.61 \cdot 10^2$	LO
2.3	ZToMuMu_NNPDF23_13TeV-pythia_M_900_13000	$2.45 \cdot 10^1$	LO
2.4	ZToMuMu_NNPDF23_13TeV-pythia_M_1300_13000	4.59	LO
2.5	ZToMuMu_NNPDF23_13TeV-pythia_M_1700_13000	1.17	LO

To combine the simulated sets for the different mass regions it is important to take into account that the edges are not sharp. Therefore, the sample starting at 500 GeV for instance also contains some events with smaller dimuon masses. To solve this issue, the dimuon mass range from 300 GeV to 13000 GeV is divided into different intervals covered by different samples resulting in a smooth dimuon mass distribution. The intervals are listed in table 3.4.

Table 3.4: Interval boundaries.

Number	Interval [GeV]
2.1	$300 - 600$
2.2	$600 - 1000$
2.3	$1000 - 1400$
2.4	$1400 - 1800$
2.5	$1800 - 13000$

In figure 3.1, two exemplary Feynman diagrams for higher order QCD contributions to the Drell–Yan process are shown. In the left one a gluon is emitted by the incoming quark, the right one shows a virtual gluon being emitted and absorbed again.

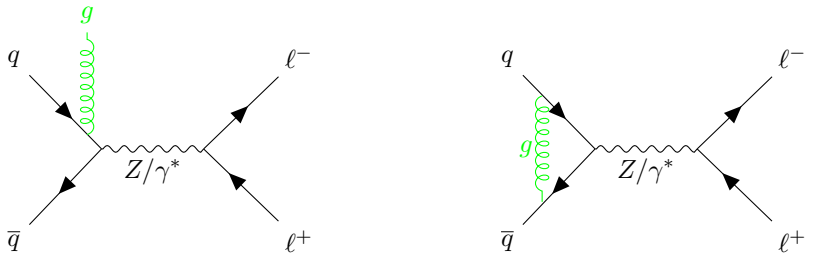

Figure 3.1: Feynman diagrams for exemplary Drell–Yan higher order contributions.

3.3 Standard Model Background Estimation

There are several standard model background processes for the Drell–Yan process that result in a final state containing a muon pair with opposite charge. In this section, all the important background processes are introduced briefly. All the samples considered are displayed at the end of this part in the tables 3.5 and 3.6.

Top Quark Backgrounds

There are three different ways the production of top quarks leads to a final state containing two muons with opposite charge that are taken into account. The top-antitop pair production, the single top production with an associated W^- boson and the complementary production of top antiquarks together with W^+ bosons. The top quark related processes form the largest contribution to the standard model background. The samples were generated using Pythia 8.2, Powheg Box V2 and nnpdf 3.0 again. For the top-antitop pair production, the process is simulated separately for different dilepton invariant mass regions.
During a gluon-gluon fusion or when a quark and an antiquark annihilate, a gluon can be produced. It can decay into a top-antitop pair further decaying into a bottom quark and a W^+ boson as well as a bottom antiquark combined with a W^-, respectively. The incurred W bosons can result in a muon pair with opposite sign, a muon neutrino and a muon antineutrino as the final state. Figure 3.2 shows the corresponding leading order Feynman diagram.

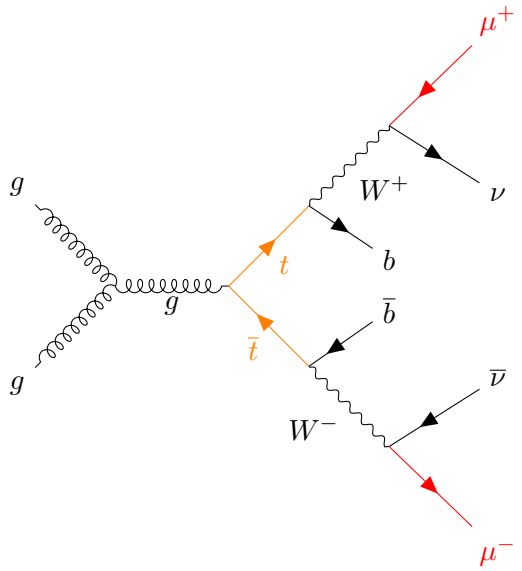

Figure 3.2: Leading order Feynman diagram for the top-antitop pair production.

The second process, the W^- associated top quark production is shown in figure 3.3. The top quark decays into a lighter quark and a W^+ boson. If the W bosons both decay further and produce a muon-antimuon pair, as displayed in figure 3.2, the signature meets the requirements.

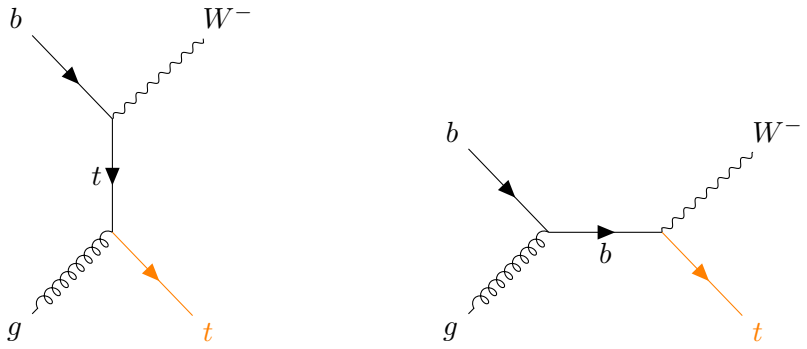

Figure 3.3: Exemplary Feynman diagrams for the W^- associated top quark production.

The third process, the W^+ associated top antiquark production, is analogous to the previous one. Two exemplary Feynman diagrams are shown in figure 3.4.

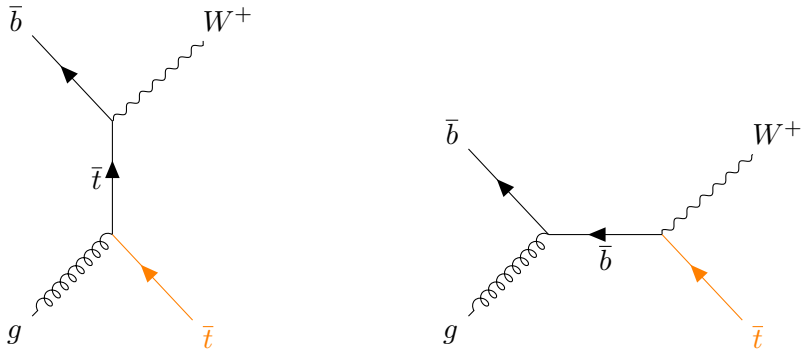

Figure 3.4: Exemplary Feynman diagrams for the W^+ associated top antiquark production.

The cross sections for the W boson associated top quark production are calculated using Top++ [37] up to NNLO while the cross sections for the top-antitop pair production is determined up to approximate NNLO in perturbative QCD.

The production of τ leptons via the Drell–Yan process can result in dimuon final states. Although there are no top quarks involved, its contribution to the dimuon mass spec-

trum is displayed together with the top quark backgrounds in section 6. To estimate the impact of this contribution, an additional Drell–Yan Monte Carlo sample (see table 3.5) considering all $q\bar{q} \to Z/\gamma^* \to \ell^+\ell^-$ processes is filtered on generator level. The sample is generated in LO using MadGraph 5 [38] and NNPDF 3.0. The cross section is calculated with Fewz 3.1b2 again applying NNLO QCD and NLO electroweak (EW) corrections.

Diboson Backgrounds

Alongside the top quark backgrounds, there are three other processes resulting in the production of two heavy gauge bosons which can further decay into muons and therefore meet the requirements: The W boson pair production, the Z boson pair production and the WZ diboson production. The W boson pair production is simulated using the same Monte Carlo generators and the same PDF set calculator as before. For the Z boson pair production and the WZ process on the other hand, only Pythia 8.2 is used for the simulation and NNPDF 2.3 is used for the PDF set. Three different Feynman diagrams for the WW production process are shown in figure 3.5. It is important to note that the quark flavour changes at the upper vertex of the t-channel diagram while q_u denotes an up-type quark, the respective Feynman diagram for down-type quarks q_d is similar. The lower Feynman diagram shows an example for gluon-induced W pair production [39].

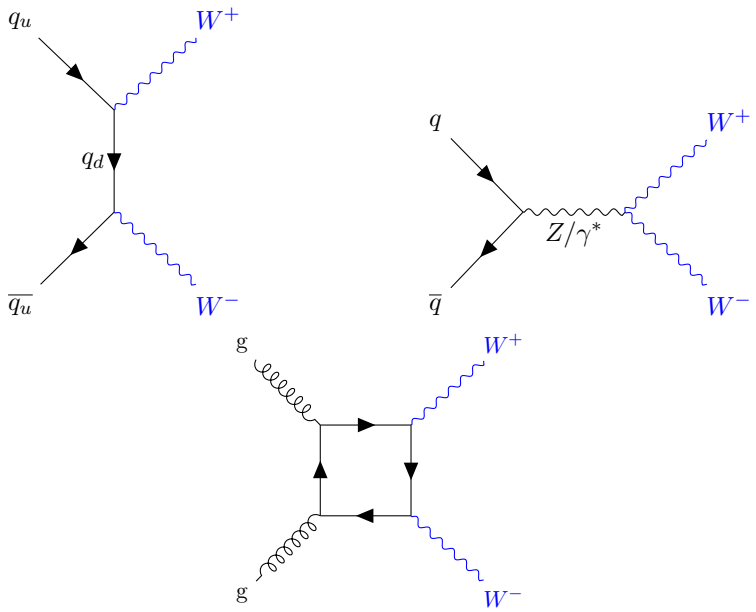

Figure 3.5: Exemplary Feynman diagrams for the W boson pair production.

Not only WW pairs are produced, but also ZZ pairs. Figure 3.6 shows two exemplary Feynman diagrams for this process.

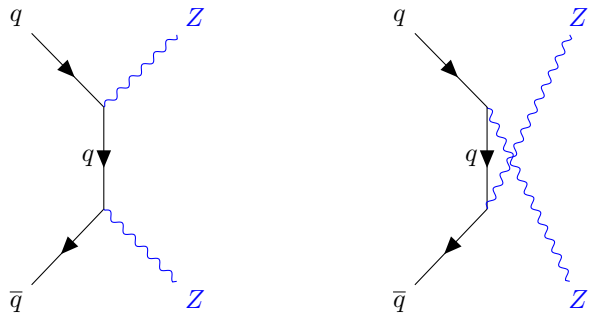

Figure 3.6: Exemplary Feynman diagrams for the Z boson pair production.

The third and last contribution to the diboson background is the production of WZ pairs. Two Feynman diagrams for this process are shown in figure 3.7. Again, the respective Feynman diagrams for down-type quarks are similar.

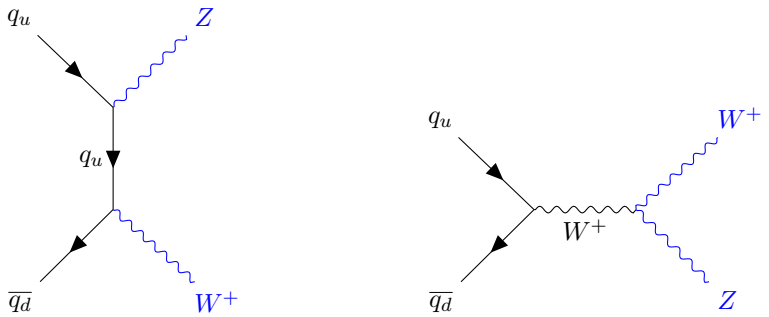

Figure 3.7: Exemplary Feynman diagrams for the WZ diboson production.

The cross sections for the diboson background samples are calculated up to NLO in QCD via MCFM [40].

Jet Backgrounds

The last background contribution discussed here are jet backgrounds. Dimuon final states arise from different processes that include at least one jet. The W-Jet contribution contains a muon from the W boson decay and another one originating from a jet. The sample has been generated by MadGraph 5 in LO and the cross section is determined up to NNLO QCD and NLO EW using FEWZ 3.1b2. For the calculation

of the PDF set NNPDF 3.0 is applied.

All contributions mainly involving hadronic interactions with dimuon final states are subsumed in the QCD background. The samples were generated in LO using PYTHIA 8.2 and NNPDF 2.3. Due to the high cross sections, 13 samples covering different regions of transverse momentum are used. To complete this section, all samples used for the standard model background estimation are displayed in the following tables 3.5 and 3.6.

Table 3.5: Background samples (1/2).

Background	Samples	σ [fb]	Precision
$t\bar{t}$	TTTo2L2Nu_TuneCUETP8M2_ttHtranche3_13TeV-powheg-pythia8	$8.73 \cdot 10^4$	NNLO
	TTToLL_MLL_500To800_TuneCUETP8M1_13TeV-powheg-pythia8	$3.26 \cdot 10^2$	NNLO
	TTToLL_MLL_800To1200_TuneCUETP8M1_13TeV-powheg-pythia8	$3.26 \cdot 10^1$	NNLO
	TTToLL_MLL_1200To1800_TuneCUETP8M1_13TeV-powheg-pythia8	3.05	NNLO
	TTToLL_MLL_1800ToInf_TuneCUETP8M1_13TeV-powheg-pythia8	$1.74 \cdot 10^{-1}$	NNLO
tW	ST_tW_top_5f_inclusiveDecays_13TeV-powheg-pythia8_TuneCUETP8M1	$3.56 \cdot 10^4$	app. NNLO
$\bar{t}W$	ST_tW_antitop_5f_inclusiveDecays_13TeV-powheg-pythia8_TuneCUETP8M1	$3.56 \cdot 10^4$	app. NNLO
DY-Jets	DYJetsToLL_M-50_TuneCUETP8M1_13TeV-madgraphMLM-pythia8	$5.77 \cdot 10^6$	NNLO
WW	WWTo2L2Nu_13TeV-powheg	$1.22 \cdot 10^4$	NNLO
	WWTo2L2Nu_Mll_200To600_13TeV-powheg	$1.39 \cdot 10^3$	NNLO
	WWTo2L2Nu_Mll_600To1200_13TeV-powheg	$5.67 \cdot 10^1$	NNLO
	WWTo2L2Nu_Mll_1200To2500_13TeV-powheg	3.56	NNLO
	WWTo2L2Nu_Mll_2500ToInf_13TeV-powheg	$5.40 \cdot 10^{-2}$	NNLO
ZZ	ZZ_TuneCUETP8M1_13TeV-pythia8	$1.65 \cdot 10^4$	NLO
WZ	WZ_TuneCUETP8M1_13TeV-pythia8	$4.71 \cdot 10^4$	NLO
W-Jets	WJetsToLNu_TuneCUETP8M1_13TeV_madgraphMLM-pythia8	$6.15 \cdot 10^7$	NNLO

Table 3.6: Background samples (2/2).

Background	Samples	σ [fb]	Precision
QCD	QCD_Pt-15to20_MuEnrichedPt5_TuneCUETP8M1_13TeV_pythia8	$3.82 \cdot 10^9$	LO
	QCD_Pt-20to30_MuEnrichedPt5_TuneCUETP8M1_13TeV_pythia8	$2.96 \cdot 10^9$	LO
	QCD_Pt-30to50_MuEnrichedPt5_TuneCUETP8M1_13TeV_pythia8	$1.65 \cdot 10^9$	LO
	QCD_Pt-50to80_MuEnrichedPt5_TuneCUETP8M1_13TeV_pythia8	$4.38 \cdot 10^8$	LO
	QCD_Pt-80to120_MuEnrichedPt5_TuneCUETP8M1_13TeV_pythia8	$1.06 \cdot 10^8$	LO
	QCD_Pt-120to170_MuEnrichedPt5_TuneCUETP8M1_13TeV_pythia8	$2.52 \cdot 10^7$	LO
	QCD_Pt-170to300_MuEnrichedPt5_TuneCUETP8M1_13TeV_pythia8	$8.65 \cdot 10^6$	LO
	QCD_Pt-300to470_MuEnrichedPt5_TuneCUETP8M1_13TeV_pythia8	$7.97 \cdot 10^5$	LO
	QCD_Pt-470to600_MuEnrichedPt5_TuneCUETP8M1_13TeV_pythia8	$7.90 \cdot 10^4$	LO
	QCD_Pt-600to800_MuEnrichedPt5_TuneCUETP8M1_13TeV_pythia8	$2.51 \cdot 10^4$	LO
	QCD_Pt-800to1000_MuEnrichedPt5_TuneCUETP8M1_13TeV_pythia8	$3.65 \cdot 10^3$	LO
	QCD_Pt-1000toInf_MuEnrichedPt5_TuneCUETP8M1_13TeV_pythia8	$1.62 \cdot 10^3$	LO

3.4 Signal Samples

As discussed in section 1.5, it is expected that the A_{fb} distribution changes considering virtual graviton exchange contributions. An ADD sample describing the interference of the virtual graviton exchange with the Drell–Yan process as well is generated in LO with Pythia 8.2 and nnpdf 2.3. Table 3.7 depicts the relevant information. The pure Drell–Yan cross section is already subtracted from the listed cross section value. The calculation is done by Pythia 8.2.

Table 3.7: Signal samples used.

Samples	Λ_T	σ [fb]
ADDGravToLL_LambdaT-5000_M-1700_13TeV-pythia8	5 TeV	2.95

3.5 Pileup Scenario

Because of the large number of particles per bunch in the storage rings of the LHC and the focusing of the beams there are multiple interactions per bunch crossing which is called "pileup". This has also be taken into account for the simulation.

The distribution of the interactions per bunch crossing for the simulation is adjusted for the behaviour of the measured data. This is done following [41] using a minimum-bias cross section of 69.2 mb. The ratio of the measured pileup distribution for the data and the estimated distribution for the simulation is calculated and used to weight the simulated events. As further explained in section 5, this results not only in a better description of the simulated processes but also in a systematic uncertainty due to the uncertainty on the value of the minimum bias cross section.

4 Event Selection

To identify interesting events and to distinguish them from others in the data sets and simulated samples presented in section 3, several conditions are established. In the following section they are introduced and explained. Because the selection is divided into different steps, each part of this section deals with one of these steps.

4.1 Trigger Selection

To identify highly energetic muon-antimuon pairs out of the numerous events recorded, single muon triggers are applied first. All of them take the whole geometrical range of the CMS muon system into account. The trigger condition requires the muon candidate to satisfy $p_{\mathrm{T}} > 50\,\mathrm{GeV}$. Furthermore, there is an additional offline cut lifting the transverse momentum treshold to 53 GeV. This cut is performed in order to avoid the trigger "turn on" behaviour. For transverse momenta close to the trigger condition treshold the trigger is not highly efficient.

4.2 Muon Tracks

After being assured that the muon candidate has a certain transverse momentum, it needs to be examined if it was both reconstructed as a tracker muon as well as a global muon. The track reconstruction is performed by the the Tune-P algorithm [42].

To identify a muon as a tracker muon only information from the inner tracking system is used for the reconstruction of the track. Either two or three hits in the pixel detectors and the silicon strip detectors are required for a valid tracker muon track. In addition, compatible hits in the muon system are also required even if only hits inside the inner tracking system are considered for the track reconstruction.

To have a valid global muon track there are several conditions to be fulfilled by the considered muon candidate. Standalone tracks are defined to be constructed only from information recorded in the outer drift chambers and resistive plate chambers. Together with the restriction that the origin of the track needs to coincide with the interaction point, possible global muon tracks are constructed by combining standalone tracks with track candidates reconstructed in the inner tracking system.

4.3 Muon Selection

Muon candidates which can be reconstructed as a tracker muon and as a global muon are required to fulfil additional criteria.

Because the inner tracking system has the best spatial resolution of the CMS detector components, the information arising from it is particularly meaningful for the track reconstruction. Muons are not only produced during the primary proton-proton collisions but can also arise from meson decays [43]. Because the vertices of these decays more

frequently lay in the outer regions of the inner tracking system, less hits are recorded in the inner tracking system in total. To reduce the contribution of such decays, the minimum number of hits in this region is increased to five. For similar reasons, it is required that at least one of the five counts in the inner tracking system occurs in the pixel detectors.

As mentioned in section 2.3, the muon system of the CMS detector is interleaved and therefore partially shielded by the flux-return yoke of the solenoidal magnet. As this shielding becomes more and more efficient towards the outermost regions of the muon system, hits in the first muon station occur more often than hits in the other stations are caused by hadronic remnants. Additionally, requiring only one layer of the muon chambers to have compatible segments with the global muon track can lead to random matches with inner tracks. To prevent these effects from distorting the result of the selection, only muon candidates that satisfy at least one of the following three additional criteria pass this step of the selection process. First, muon candidates with matching segments in two or more different stations pass this selection step. Moreover, if the only station to match is not the first layer, the muon candidate also passes. If the only station matching is the first one, but there are at least two compatible measurements from resistive plate chambers, the third criterion is fulfilled.

The distance d_{xy} from the track fitted by the Tune-P algorithm to the primary vertex in the x-y plane needs to be smaller than 0.2 cm. An important purpose of this condition is to reject cosmic muons.
Even though the tracks and therefore the results for the transverse momenta reconstructed by the Tune-P algorithm are reliable in the most cases, there are still some anomalies. They are rejected applying the criterion that the relative uncertainty on p_{T} should be smaller than 0.3.

The last condition explained in this part is requiring the muon candidate to be relatively isolated inside the inner tracker. To define the relative isolation, the scalar sum of the transverse momenta of all the tracks located inside a cone around the inner track of the respective muon is calculated. The cone is defined by $\Delta R < 0.3$. The sum of the transverse momenta inside the cone divided by the transverse momentum of the considered muon is required to be 0.1 or less.

4.4 Dimuon Selection

In the previous part, several conditions were introduced to ensure that the selected events actually contain at least one muon. In this last part of the event selection, criteria are presented to identify possible pairs.

First, the pair candidate needs to be a muon-antimuon pair and therefore a muon candidate with negative charge is required as well as a muon candidate with positive charge.

Furthermore, one of the two verified muons needs to be compatible with the high level trigger (HLT) object. This is guaranteed by claiming that their tracks are situated inside a cone with $\Delta R < 0.2$.

To further reduce the contribution of cosmic muons, a cut on the opening angle between the muon direction and the antimuon direction is applied. All candidates fulfilling $\measuredangle(\mu_1\mu_2) < \pi - 0.02$ meet the requirements. This claim corresponds to a treshold of $\cos(\measuredangle(\mu_1\mu_2)) = \cos(\pi - 0.02) \approx -0.9998$.

The last criterion that is applied to ensure that two verified muons form a muon pair indeed is especially pertinent to the signal analysis. The theory considered in section 1.5 claims that the hypothetical graviton can decay into a muon pair and therefore the two muons should share a common vertex. To quantify the compatibility of the two muon tracks with a common vertex, a vertex fit [44] is applied. In general, if the considered event contains more than one muon pair that fulfils all of the aforementioned criteria, the pair with the highest invariant mass $M_{\mu\mu}$ is used for the further analysis.

5 Systematic Uncertainties

In advance of presenting the results of the analysis in the sections 6-8 the systematic uncertainties considered for this thesis are calculated. This section is divided into two parts. In the first part, the different sources of systematic uncertainties are introduced and explained further, in the second part their relative impact on the event yield is discussed.

5.1 Overview of the different Systematic Uncertainties

Pileup

As already elucidated in section 3.5, a pileup correction is applied to the Monte Carlo simulations. The measured value of 96.2 mb for the minimum bias cross section has an uncertainty of 5% [41]. The value is shifted up and down by its uncertainty and the pileup distribution is recalculated with these shifted values. To symmetrize the uncertainty, the ratio R_k^{pileup} is determined per bin.

$$R_k^{\text{pileup}} = \frac{1}{2}\left(\left|1 - \frac{{H^+}_k}{{H^0}_k}\right| + \left|1 - \frac{{H^-}_k}{{H^0}_k}\right|\right) + 1 \tag{5.1}$$

Here, ${H^0}_k$ denotes the original histogram entries and $H_k^{\pm}$ the entries of the shifted histograms.

Muon $p_{\mathbf{T}}$ Scale

The measured muon tracks depend on the alignment of the detector components. Following [42], the curvature bias can be expressed as a constant k_b added to the charge over transverse momentum ratio at lowest order.

$$\frac{q}{p_{\text{T}}} \rightarrow \frac{q}{p_{\text{T}}} + k_b \tag{5.2}$$

To determine the optimal value for k_b, data events are used to a create a q/p_{T} distribution which is compared to the distribution of the simulation with different biases k_b applied. Only muons fulfilling $p_{\text{T}} > 200\,\text{GeV}$ and $|\eta| < 2.1$ or $p_{\text{T}} > 120\,\text{GeV}$ and $2.1 < |\eta| < 2.4$ are considered. To find the optimum bias k_b^{opt} in different regions of rapidity and for different azimuthal angle intervals, χ^2 minimizations are performed. The bias is assumed to follow a Gaussian distribution with mean k_b^{opt} and standard deviation σ_{k_b}. The results are used to analyse the impact of the bias on the dimuon mass distribution.

Muon $p_{\mathbf{T}}$ Resolution

In order to compare the transverse momentum resolution for the data events and the

simulation, boosted Z bosons are used. The measured and the simulated mass spectra are subdivided according to the transverse momenta of the respective events [45]. For each of the spectra, the Z boson mass peak is then fitted to obtain its width. The outcomes are different for the data and the simulation, resulting in an uncertainty on the simulated event yield.

Muon Reconstruction and Selection

To quantify the differences between the measurement and the simulation concerning the reconstruction and selection of muons, the tag-and-probe method is applied [45]. To "tag" an event, a muon fulfilling the selection criteria introduced in the sections 4.1-4.3 except for the isolation criterion is required. The remaining muons contained in the event "probe" the reconstruction and selection and are therefore used to determine the efficiencies in equation 5.3. Both "tag" and "probe" muon have to fulfil several additional criteria, especially concerning their isolation and spatial separation.

$$\epsilon = \epsilon_{\text{Standalone}} \times \epsilon_{\text{Global}} \times \epsilon_{\text{Muon Sel.}} \tag{5.3}$$

All efficiencies are defined as ratios between the number of events that pass the selection process and the total number of events that passed all former selection steps. $\epsilon_{\text{Standalone}}$ and ϵ_{Global} refer to the muon track reconstruction described in section 4.2 while $\epsilon_{\text{Muon Sel.}}$ corresponds to the requirements explained in section 4.3 only applied for the measurements with the muon system. ϵ differs for the simulation and the measured data. The resulting systematic uncertainty is given as a function of the rapidity and the transverse momentum of the muon.

Parton Distribution Functions

As already mentioned in section 3, the parton distribution functions (PDFs) need to be calculated to simulate standard model processes occurring in proton-proton collisions. Following [46], $N = 100$ replicas of the PDF set used are calculated, resulting in N different values for the respective cross section σ of the simulated processes. The results are arranged in ascending order:

$$\sigma^{(1)} \leq \sigma^{(2)} \leq ... \leq \sigma^{(N-1)} \leq \sigma^{(N)}. \tag{5.4}$$

The PDF uncertainty is then calculated via

$$\delta^{\text{pdf}}\sigma = \frac{\sigma^{(84)} - \sigma^{(16)}}{2}, \tag{5.5}$$

which corresponds to the 68% confidence level interval.

Mass independent Uncertainties

In addition to the aforementioned uncertainties that depend for example on the interaction scale, there are also mass independent uncertainties. Although their contribution is of minor importance for this thesis, as they cancel out in the calculation of A_{fb}, they have an impact on the results of the analysis presented in section 6. The uncertainty in the determination of the total integrated luminosity arises to 2.5% [29], while a flat uncertainty of 7% is [47] assigned on the cross sections for the simulated standard model processes except for the muon pair production via the Drell-Yan process. In addition to that there is a difference in the trigger efficiency for the measurement and the simulation, resulting in a systematic uncertainty of 0.4% on the event yield [47].

5.2 Impact of the Systematic Uncertainties

In section 7 the Drell–Yan forward-backward asymmetry parameter A_{fb} is derived as a function of the dimuon invariant mass. In the first part of section 7 the following mass bin edges are used (GeV): $300, 350, 400, 450, 500, 550, 600, 650, 700, 800, 900, 1000, 1200, 1500, 2300$. For reasons of clarity, this mass binning is called binning A for the rest of this thesis. To obtain comparable results, it is also applied in the first part of this section. Considering only Drell–Yan events, figure 5.1 shows the ratio between the shifted and the original simulated distributions for all systematic uncertainty contributions that depend on the dimuon mass.

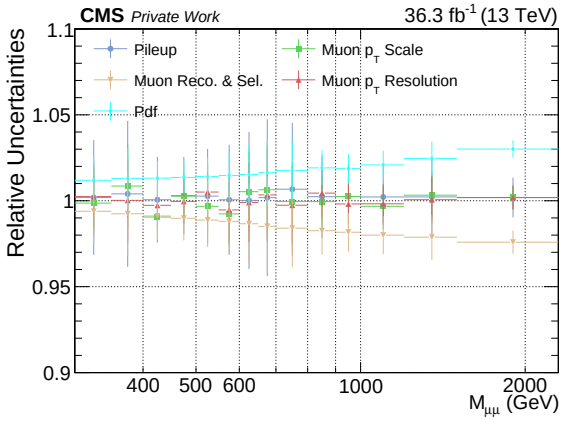

Figure 5.1: Relative impact of different systematic uncertainties for Drell–Yan events applying binning A.

.

Figure 5.1 shows that all contributing systematic uncertainties are below 5% in the complete dimuon mass range covered. The pileup contribution, the muon p_{T} resolution uncertainty and the muon p_{T} scale uncertainty do not exceed 1%. The muon reconstruction and selection uncertainty reaches values above 2% beyond 1 TeV. For dimuon

masses above 1500 GeV the PDF uncertainty is the dominant contribution while the flat uncertainty on the total integrated luminosity, which is not displayed in figure 5.1, dominates in the mass region below 1500 GeV. Figure 5.2 depicts the corresponding distribution for standard model background events.

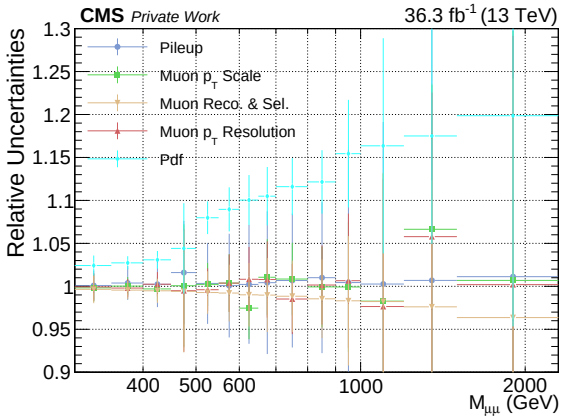

Figure 5.2: Relative impact of different systematic uncertainties for standard model background events applying binning A.

Figure 5.2 shows that the contributing uncertainties still have ratio values mostly between 0.95 and 1.05. Nevertheless, the uncertainties are significantly larger in comparison to 5.1. For dimuon masses above 600 GeV PDF uncertainties above 10% are common. In the $1000 - 1200$ GeV mass bin the muon p_{T} scale uncertainty and the muon p_{T} resolution contribution exceed 5%. The muon reconstruction and selection contribution becomes less important in comparison to the PDF uncertainty but also increases. It is also noticeable that the variation of the systematic uncertainties is larger than in figure 5.1. This behaviour is associated with the low number of events per bin in the high mass region, which results in large statistical uncertainties further propagating on the systematic uncertainties. The ratio highly depends on single events, which can result in large systematic uncertainties for single bins.
In the second part of section 7 the forward-backward asymmetry parameter A_{fb} is derived using another mass binning for a better comparison to former results for the A_{fb} distribution [11], [48]. This mass binning is called binning B for the rest of this thesis, again for reasons of clarity. The dimuon mass range considered is $76 - 2000$ GeV and the mass bin edges are (GeV): $76, 81, 86, 91, 96, 101, 106, 110, 115, 120, 126, 133, 141, 150, 160, 171, 185, 200, 220, 243, 273, 320, 380, 440, 510, 600, 700, 830, 1000, 1200, 1500, 2000$. Binning B is applied for the rest of this section. In section 1.4 forward events were defined via $\cos(\theta_{\mathrm{CS}}) > 0$ where θ_{CS} denotes the polar angle in the Collins–Soper frame. Only considering Drell–Yan forward events, figure 5.3a depicts the relative impact of the systematic uncertainties again while figure 5.3b is the analogon for backward events with $\cos(\theta_{\mathrm{CS}}) < 0$.There are no noticeable differences in comparison to figure 5.1 for masses above 300 GeV.

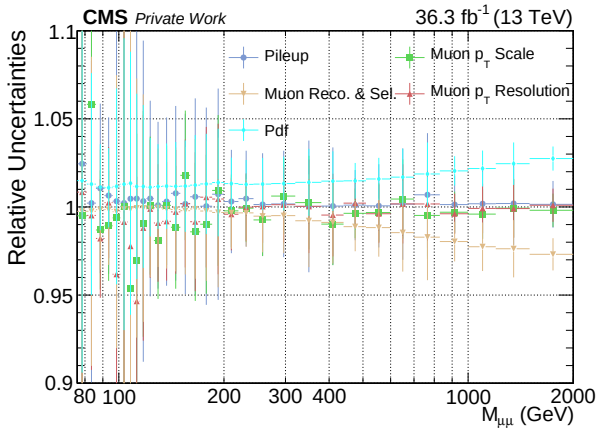

(a) Forward events ($\cos(\theta_{\mathrm{CS}}) > 0$)

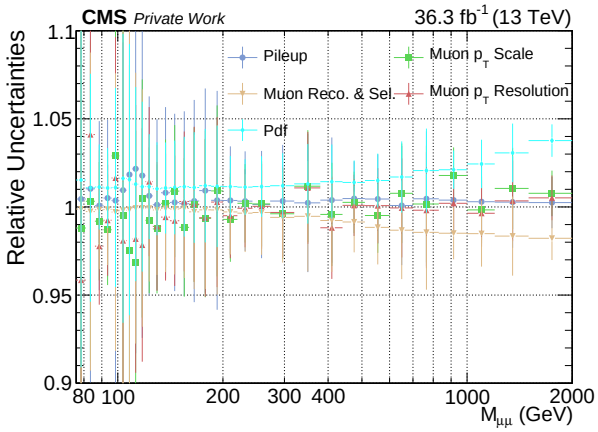

(b) Backward events ($\cos(\theta_{\mathrm{CS}}) < 0$)

Figure 5.3: Relative impact of different systematic uncertainties for Drell–Yan events applying binning B.

Several bins in the mass region below 200 GeV have dominant uncertainties around 5% and the variation of the systematic uncertainties is high in this region. Again, this is caused by the low number of events in the respective bins. Figure 5.4 shows the analogous distributions for standard model background events. There are no major differences compared to 5.2.

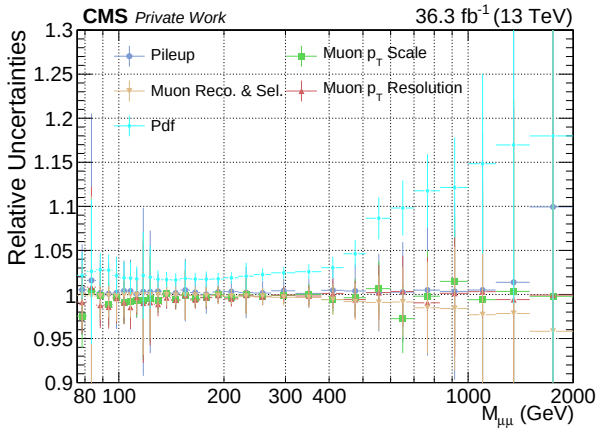

(a) Forward events ($\cos(\theta_{\mathrm{CS}}) > 0$)

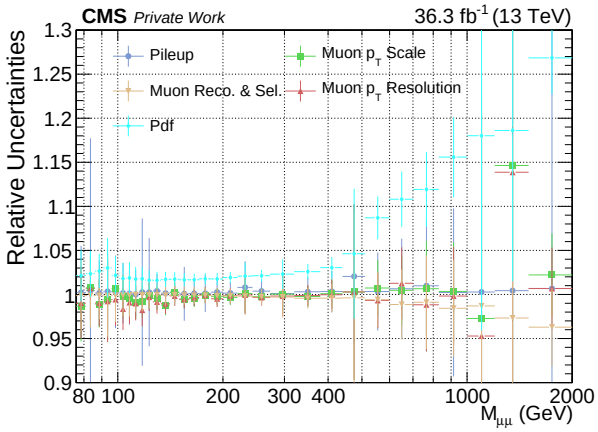

(b) Backward events ($\cos(\theta_{\mathrm{CS}}) < 0$)

Figure 5.4: Relative impact of different systematic uncertainties for standard model background events applying binning B.

6 Dimuon Mass Distributions

In the following section the results of the applied event selection are presented. The kinematic distributions shown are further employed in the next section to determine the forward-backward asymmetry parameter A_{fb} for the data set and the Monte Carlo simulations. Figure 6.1 depicts the dimuon mass distribution for the data and for different simulated standard model contributions using binning B. As already mentioned the reason for this choice lies in the better comparability with earlier results for the asymmetry parameter A_{fb} as a funtion of the dimuon invariant mass in section 7.

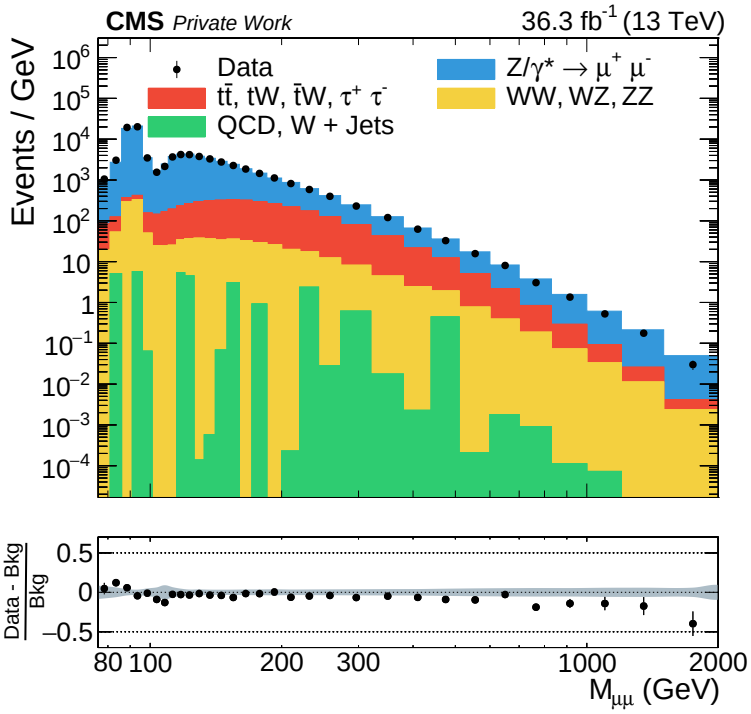

Figure 6.1: The dimuon mass distribution for invariant masses between 76 GeV and 2000 GeV using binning B.

Figure 6.1 clearly shows that Drell–Yan events constitute the largest contribution of the simulated processes, followed by the top quark backgrounds. The diboson processes also form a significant background while the last category considered in section 3.3, the jet backgrounds, clearly represent the smallest contribution. The Z peak is unequivocally discernible at around 90 GeV. The event count per GeV has a minimum above the Z peak and also decreases rapidly for smaller dimuon masses. The reason for this behaviour is the trigger selection described in section 4.1 as muon candidates are required to fulfil $p_T > 53\,\mathrm{GeV}$. Therefore, the amount of muon pairs with a dimuon mass around the Z peak is considerably reduced.

The systematic uncertainties are displayed as a grey band around the zero line in the lower subplot. The overall agreement between data and Monte Carlo simulations of the standard model background within the uncertainties is observed to be good, but the lower subplot particularly emphasizes that there is a deficit of data events considering the high mass region which was already measured with CMS for this spectrum [49]. To exclude possible experimental issues causing the deficit, studies on the L1 and HLT trigger efficiencies were performed and the muon reconstruction process was probed in detail.

Figure 6.2 shows the dimuon mass distribution for forward events ($\cos(\theta_{\mathrm{CS}}) > 0$) and backward events ($\cos(\theta_{\mathrm{CS}}) < 0$) using the same mass binning than figure 6.1. Because the jet background contributions become even smaller due to the allocation applied, they are displayed together with the diboson backgrounds.

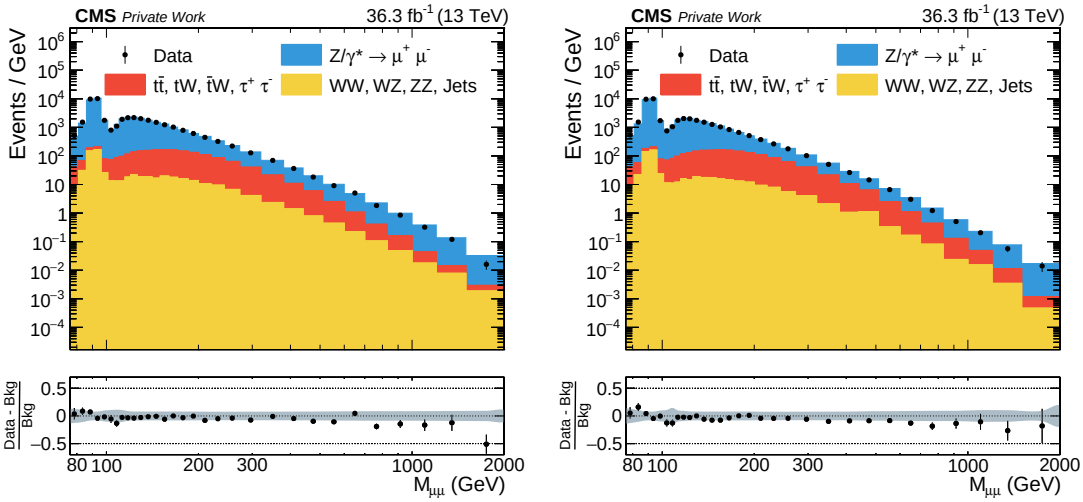

(a) Forward events ($\cos(\theta_{\mathrm{CS}}) > 0$)

(b) Backward events ($\cos(\theta_{\mathrm{CS}}) < 0$)

Figure 6.2: The dimuon mass distribution for forward and backward events using binning B.

The Z peak is clearly visible and the distribution has the shape of the total dimuon mass distribution as expected. Although there are no significant deviations observed from the standard model in the low mass regime, the lower subplot depicts a deficit of data events again for high masses.

The main goal of this thesis is the calculation of the angular forward-backward asymmetry parameter A_{fb} as a function of the dimuon mass. Therefore, last part of this section deals with the $\cos(\theta_{\mathrm{CS}})$ distribution, where θ_{CS} denotes the polar angle in the Collins–Soper frame. Figure 6.3 shows the $\cos(\theta_{\mathrm{CS}})$ distribution in two different dimuon mass regions.

In figure 6.3a the $\cos(\theta_{\mathrm{CS}})$ distribution is depicted for dimuon masses near the Z boson mass peak, where A_{fb} is expected to be close to zero. The Drell–Yan contribution to the standard model simulation clearly dominates and the agreement between the simulation and the measurement is observed to be good. The distribution is symmetric and therefore matches the expectation.
Figure 6.3b shows the $\cos(\theta_{\mathrm{CS}})$ distribution for dimuon masses between 440 GeV and 510 GeV. While the agreement between the measured events and the simulation is reasonable for $|\cos(\theta_{\mathrm{CS}})| < 0.5$, deviations are observed for larger $|\cos(\theta_{\mathrm{CS}})|$. The A_{fb} parameter is expected to be large and positive in this dimuon mass region. Indeed, there are clearly more forward events than backward events observed for the Drell–Yan process.

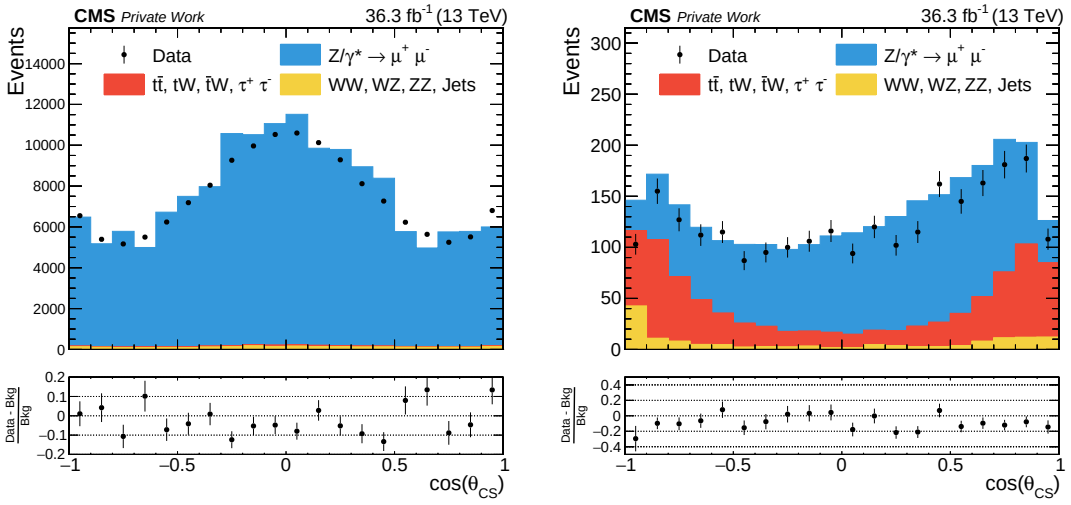

(a) 86 GeV $< M_{\mu\mu} <$ 96 GeV (b) 440 GeV $< M_{\mu\mu} <$ 510 GeV

Figure 6.3: $\cos(\theta_{\mathrm{CS}})$ distribution in two different dimuon mass regions.

7 Measured and Simulated Forward-Backward Asymmetry

In section 3.2 the different simulated samples and data sets considered have been presented. This section is divided into three parts. In the first part the forward-backward asymmetry parameter A_{fb} is determined for the LO Drell–Yan simulation generated by Pythia 8.2 and the Drell–Yan simulation up to NLO QCD generated by Powheg Box V2.0 (Pythia 8.2 still handling hadronization and parton showering). This part aims to evaluate the influence of the NLO contribution to A_{fb}.
In the second part the A_{fb} distributions for the LO and the NLO simulation are compared separately to the measurement to examine if the NLO simulation describes the measured data significantly better. Defined in section 5.2, binning A is used in the first two parts of this section. It is chosen to allow for the intended comparisons in a wide dimuon mass range. Because the LO Drell–Yan simulation only provides results for dimuon masses above 300 GeV, lower values are omitted.
In the third part detailed studies of the A_{fb} parameter for the measured data and the simulation are provided in four different regions of absolute rapidity also including the impact of the systematic uncertainties determined in section 5 on the event yield.

7.1 Comparison of the LO and the NLO Drell–Yan Simulation

Figure 7.1 shows the A_{fb} distribution for both the LO and the NLO Drell–Yan simulation.

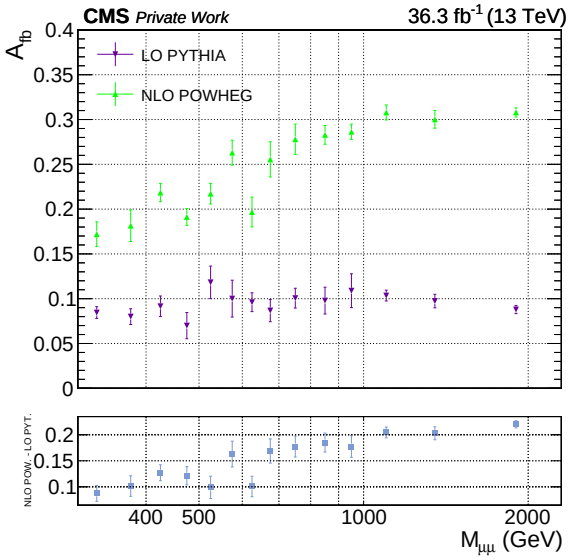

Figure 7.1: The forward-backward asymmetry parameter A_{fb} for the LO and the NLO Drell–Yan simulation between 300 GeV and 2300 GeV using binning A.

The predictions by the respective simulations are not compatible. It is also a prominent feature in figure 7.1 that A_{fb} appears to converge to a positive value in the high mass regime for both the LO and the NLO simulation. To further examine this phenomenon, figure 7.2 depicts the respective predictions for A_{fb} between invariant masses of 3 TeV and 13 TeV using the following mass bin edges (GeV): 2300, 3500, 4000, 4500, 5000, 6000, 7000, 8000, 9000, 10000, 11000, 12000, 13000.

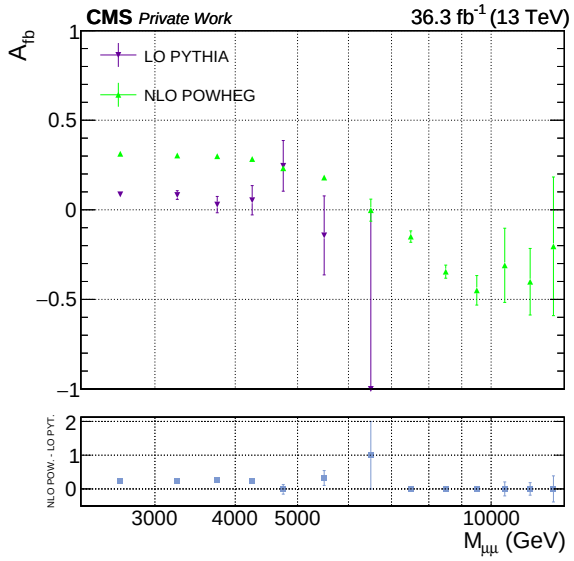

Figure 7.2: The forward-backward asymmetry parameter A_{fb} for the LO and the NLO Drell–Yan simulation between 2300 GeV and 13000 GeV using binning A.

For the LO Drell–Yan simulation, figure 7.2 does not contradict the statement that the A_{fb} parameter stays constant in the high mass regime. In the region between 3 TeV and 5 TeV it fluctuates around 0.1, while the subsequent two mass bins do not provide statistically reliable statements because there are too few simulated events.

For the NLO Drell–Yan simulation, figure 7.2 shows that A_{fb} decreases for dimuon masses beyond 3 TeV and therefore does not stay constant in the high mass regime. Furthermore, the distribution crosses the zero line between 6 TeV and 7 TeV and declines to roughly -0.45 between 9 TeV and 10 TeV. Following the discussion in section 1.3, the considered theoretical calculations predict A_{fb} converging to a positive value for dimuon masses beyond 500 GeV. A more extensive theoretical approach that allows for an accurate description of the forward-backward asymmetry in the very high mass regime is beyond the scope of this thesis. To obtain a deeper understanding of the observed behaviour, detailed studies of the POWHEG BOX V2.0 generator and the PDF set used would have to be performed.

Figure 7.3 shows the $\cos(\theta_{\mathrm{CS}})$ distribution for the $9 - 10$ TeV mass bin. While sta-

tistical fluctuations are observed, a clear trend to negative values can be seen. Because the majority of the entries fulfils $\cos(\theta_{\mathrm{CS}}) < 0$ it is reasonable that the A_{fb} parameter is large and negative in this mass bin.

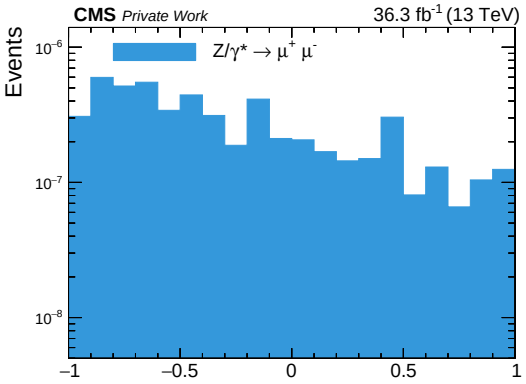

Figure 7.3: $\cos(\theta_{\mathrm{CS}})$ distribution for the NLO Drell–Yan simulation between 9 TeV and 10 TeV.

7.2 Comparison of the LO and the NLO Simulation with the Measurement

The contributions of all simulated standard model processes introduced in section 3 except for the dimuon pair production via the Drell–Yan process are subtracted from the measurement. The resulting A_{fb} distribution is compared to the distribution for the LO Drell–Yan simulation in figure 7.4 for dimuon masses between 300 GeV and 2300 GeV. The sum of all standard model contributions including the Drell–Yan process is denoted as "MC" for the rest of this thesis.

The highest dimuon invariant mass measured is 2300 GeV and there are only a few events recorded nearby this treshold. Therefore, assuming the measured event yield following a Poisson distribution results in a large variation of the measured A_{fb} values in the high mass regime. Nevertheless, the LO Drell–Yan simulation clearly does not describe the measured data accurately since A_{fb} is larger for the measurement in every mass bin.

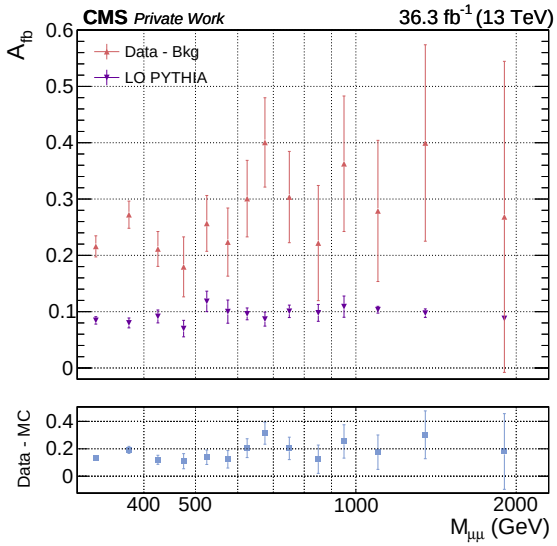

Figure 7.4: A_{fb} for the LO Drell–Yan simulation and the measurement between 300 GeV and 2300 GeV using binning A.

Using the same mass binning, figure 7.5 shows the A_{fb} distribution for the measurement compared with the NLO Drell–Yan simulation. All measured data points are compatible with the NLO Drell–Yan simulation.

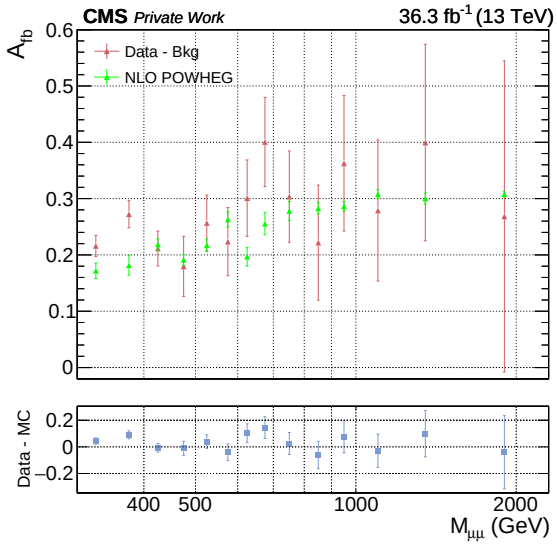

Figure 7.5: A_{fb} for the NLO Drell–Yan simulation and the measurement between 300 GeV and 2300 GeV using binning A.

7.3 Detailed Study of A_{fb} in four Rapidity Bins

Figure 7.6 shows A_{fb} for all considered standard model processes and the measurement as a function of the dimuon invariant mass in four different regions of absolute rapidity (of the dimuon system): $0 < |y| < 1$, $1 < |y| < 1.25$, $1.25 < |y| < 1.5$ and $1.5 < |y| < 2.4$. Introduced in section 5.2, mass binning B is used while the bins in the high mass regime between 830 GeV and 2000 GeV are combined such that at least five data events in both the forward and the backward region contribute to the calculation of A_{fb} .

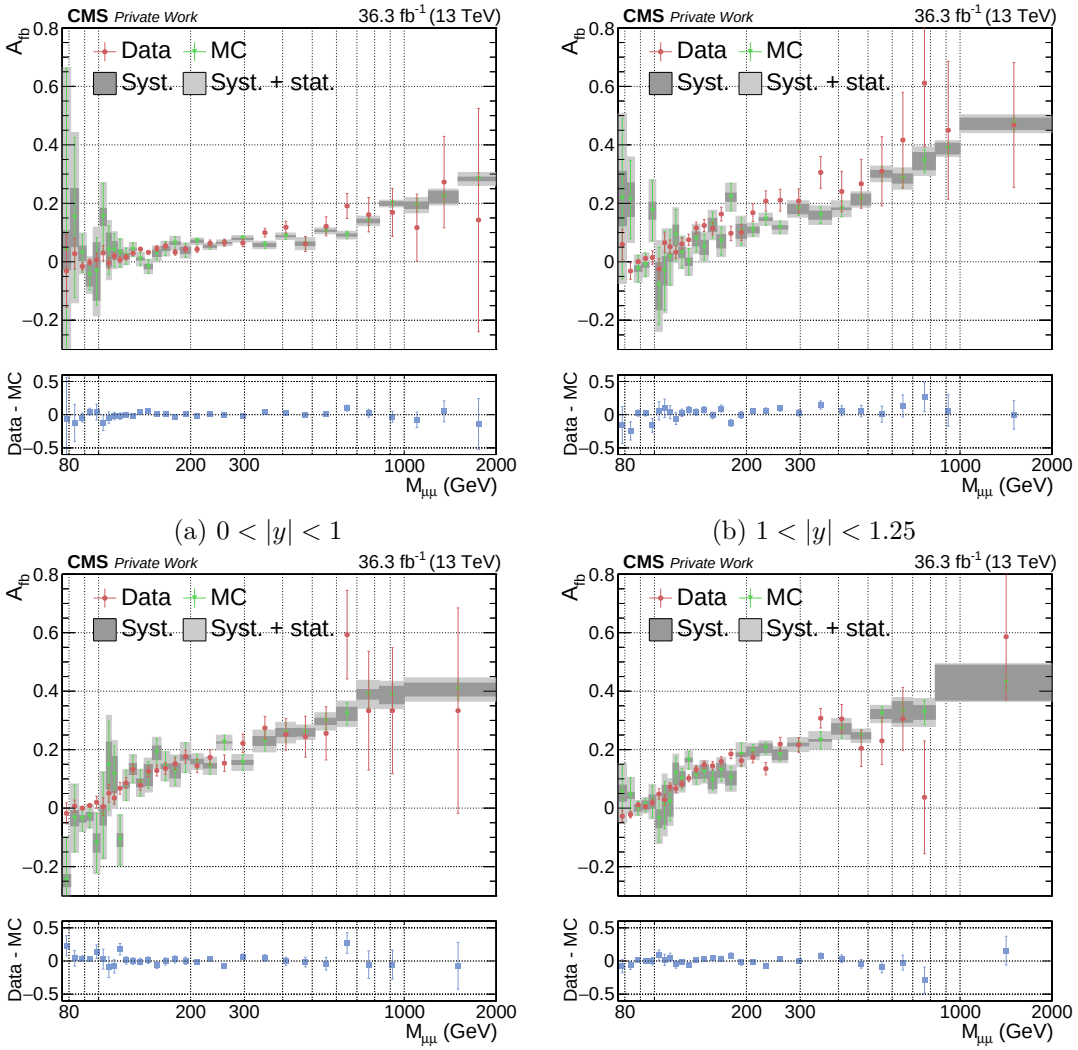

(a) $0 < |y| < 1$

(b) $1 < |y| < 1.25$

(c) $1.25 < |y| < 1.5$

(d) $1.5 < |y| < 2.4$

Figure 7.6: A_{fb} distributions in four ranges of absolute rapidity for the measurement and the standard model simulation between 76 GeV and 2000 GeV.

The systematic uncertainties and the combined systematic and statistical uncertainties are represented by dark grey and light grey rectangles, respectively. The uncertainties depicted in the lower subplots are calculated based on the statistical uncertainties while the data is assumed to follow a Poisson distribution.

The Drell–Yan events constitute the dominant contribution to the simulated standard model events (see figure 6.1). Therefore, the A_{fb} distributions for the simulation follows the Drell–Yan characteristic shape described in section 1.3, with A_{fb} values close to zero in the Z boson mass peak region and positive values for larger dimuon masses.

To quantify the agreement between measured data and simulation n_σ is calculated via

$$n_\sigma = \frac{|A_{\mathrm{fb}}^{MC} - A_{\mathrm{fb}}^{dat.}|}{\sqrt{\sigma_{\mathrm{dat.}}^2 + \sigma_{\mathrm{tot.}}^2}} \tag{7.1}$$

while $\sigma_{\mathrm{tot.}}$ is determined by combining the systematic and statistical uncertainties on the simulation. For most mass bins $n_\sigma < 1.2$ holds true. Larger deviations occur in single mass bins throughout the whole dimuon mass range and for all regions of absolute rapidity (see table 7.1), but rarely for consecutive bins. Two bins next to each other with a greater deviation are observed for $0 < |y| < 1$ between 133 GeV and 150 GeV and for $1.25 < |y| < 1.5$ between 243 GeV and 320 GeV.

Table 7.1: Values of n_σ for different mass bins (corresponding to figure 7.6).

$\lvert y\rvert$ region	Bin range (GeV)	n_σ
$0 < \lvert y\rvert < 1$	$133 - 141$	1.4
	$141 - 150$	1.9
	$200 - 220$	1.8
	$320 - 380$	2.2
	$700 - 830$	1.5
$1.25 < \lvert y\rvert < 1.5$	$76 - 81$	1.5
	$96 - 101$	1.3
	$115 - 120$	2.0
	$243 - 273$	1.9
	$273 - 320$	1.6
	$600 - 700$	1.7

(a) / (c)

$\lvert y\rvert$ region	$M_{\mu\mu}$ (GeV)	n_σ
$1 < \lvert y\rvert < 1.25$	$81 - 86$	1.7
	$96 - 101$	1.5
	$126 - 133$	1.4
	$171 - 185$	2.7
$1.5 < \lvert y\rvert < 2.4$	$126 - 133$	1.9
	$171 - 185$	1.7
	$220 - 243$	2.2
	$320 - 380$	1.7
	$700 - 830$	1.5

(b) / (d)

Considering figure 7.6 and table 7.1 no significant deviations between the measured A_{fb} distribution and the standard model prediction are observed.

Figure 7.7 depicts the A_{fb} distributions for the NLO Drell–Yan simulation, therefore the standard model background contributions are subtracted from the measurement. The corresponding distributions at generator level can be found in the appendix, illustrating the small impact of detector resolution and acceptance.

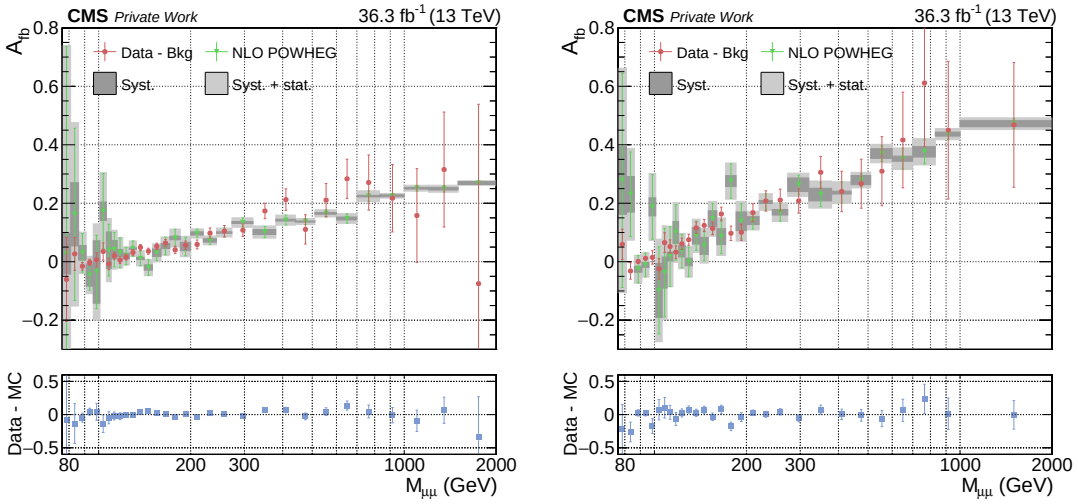

(a) $0 < |y| < 1$

(b) $1 < |y| < 1.25$

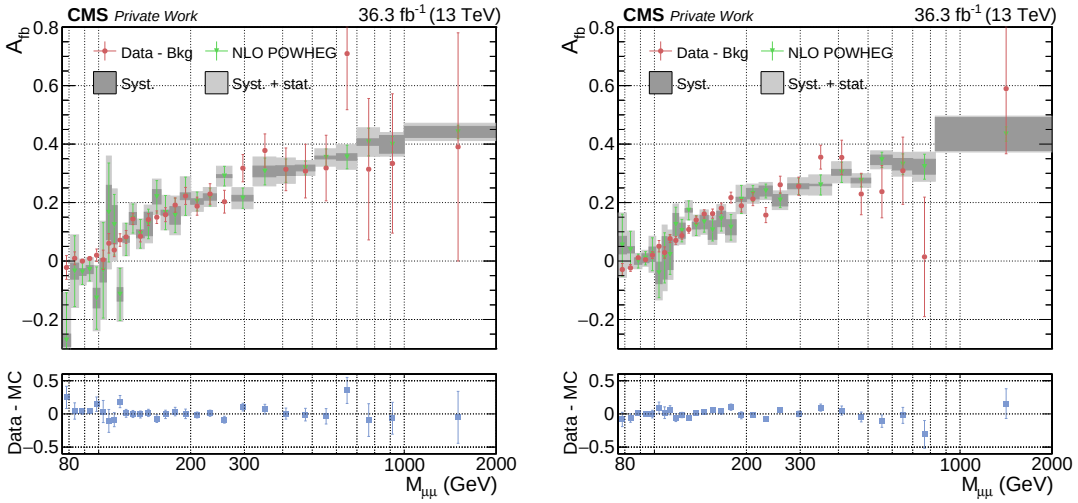

(c) $1.25 < |y| < 1.5$

(d) $1.5 < |y| < 2.4$

Figure 7.7: A_{fb} distributions in four ranges of absolute rapidity for the measurement (the simulated backgrounds are subtracted) and the NLO Drell–Yan simulation between 76 GeV and 2000 GeV.

Table 7.3 shows the respective values for n_σ only considering bins with $n_\sigma > 1.2$. There are no remarkable differences in comparison to figure 7.6.

Table 7.3: Values of n_σ for different mass bins (corresponding to figure 7.7).

$\lvert y\rvert$ region	Bin range (GeV)	n_σ
$0 < \lvert y\rvert < 1$	$133 - 141$	1.4
	$141 - 150$	1.9
	$200 - 220$	1.7
	$320 - 380$	2.1
	$700 - 830$	2.0
$1.25 < \lvert y\rvert < 1.5$	$76 - 81$	1.5
	$96 - 101$	1.3
	$115 - 120$	2.0
	$243 - 273$	1.7
	$273 - 320$	1.7
	$600 - 700$	1.8

(a) / (c)

$\lvert y\rvert$ region	$M_{\mu\mu}$ (GeV)	n_σ
$1 < \lvert y\rvert < 1.25$	$81 - 86$	1.6
	$96 - 101$	1.5
	$126 - 133$	1.4
	$171 - 185$	2.7
$1.5 < \lvert y\rvert < 2.4$	$126 - 133$	1.9
	$171 - 185$	1.9
	$220 - 243$	2.1
	$320 - 380$	1.8
	$700 - 830$	1.5

(b) / (d)

The A_{fb} distributions presented in figure 7.6 are in good agreement with recent results obtained by the CMS collaboration [50]. A_{fb} is observed to be close to zero around the Z boson mass peak. Between 100 GeV and 200 GeV the values increase to roughly 0.1 and 0.2 for $0 < |y| < 1$ and $1 < |y| < 2.4$, respectively. For higher dimuon masses A_{fb} further increases to 0.4 for $1 < |y| < 2.4$ and 0.3 for $0 < |y| < 1$. A direct comparison between the distributions can be found in figures 10.2 and 10.3 in the appendix.

8 Forward-Backward Asymmetry for ADD Model Signals

As discussed in section 1.5 the A_{fb} distribution is expected to change assuming virtual graviton exchange as an additional contributing process. In this section the A_{fb} distribution for the signal sample is presented and compared to the results for the standard model simulation and the measurement. Figure 8.1 shows A_{fb} as a function of the dimuon mass for the simulation and the signal. The mass binning previously utilized in figure 7.2 is used.

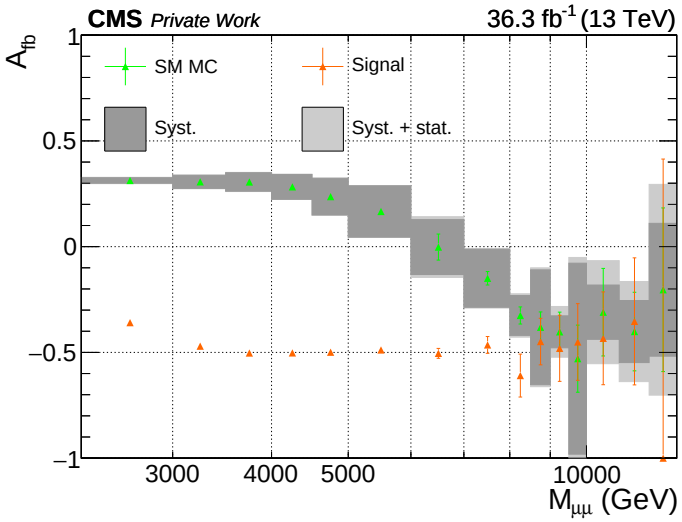

Figure 8.1: A_{fb} as a function of the dimuon mass between 2300 GeV and 13000 GeV for the signal and the standard model simulation.

Figure 8.1 clearly indicates the potential of A_{fb} to disentangle standard model and ADD contributions to the Drell–Yan process. For this analysis, signal events are only produced for dimuon masses beyond 1700 GeV and data events are only available for dimuon masses below 2300 GeV. In the remaining region, A_{fb} is heavily influenced by single data events, resulting in large statistical uncertainties. Therefore, a comparison between the A_{fb} distributions for the signal and the data can not be utilized to reliably exclude the ADD model of large extra dimensions with $\Lambda_T = 5000$ GeV. Nevertheless, A_{fb} is depicted in figure 8.2 for the measurement, the standard model simulation and the simulated signal in two mass bins: $1700 - 2000$ GeV and $2000 - 2300$ GeV.

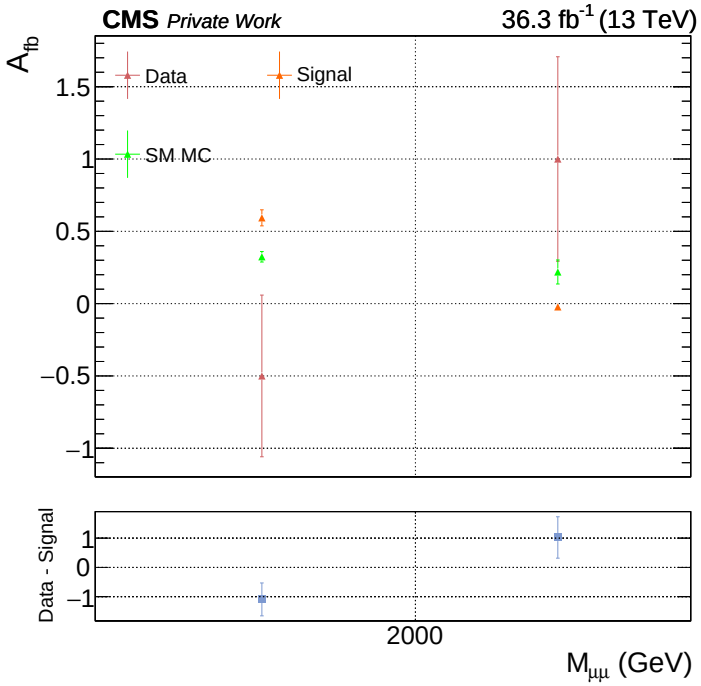

Figure 8.2: A_{fb} as a function of the dimuon mass between 1700 GeV and 2300 GeV for the measurement, the simulated signal and the standard model simulation.

9 Conclusion

In this thesis the forward-backward asymmetry of Drell–Yan muon pairs produced in proton-proton collisions at the LHC has been determined. The analysis is based on the measurements by the CMS experiment during the 2016 data taking period corresponding to a centre-of-mass-energy of $\sqrt{s} = 13\,\text{TeV}$. The total integrated luminosity is $\mathcal{L} = 36.3\,\text{fb}^{-1}$.

Selection criteria for the events considered in the analysis have been discussed as well as the different systematic uncertainties and their impact on the event yield. The forward-backward asymmetry parameter has been calculated as a function of the dimuon invariant mass for Drell–Yan simulations in LO and NLO, while the NLO simulation was observed to describe the measured data significantly better. Furthermore, a detailed study of A_{fb} in four regions of absolute rapidity has been presented. The distributions of the measurement were compared to the SM simulation. No significant deviations from the SM predictions have been observed.

The A_{fb} distribution has been determined also considering the virtual graviton exchange predicted by the ADD model of large extra dimensions. Clear indications for the potential of A_{fb} to distinguish between SM and virtual graviton exchange contributions were observed.

10 Appendix

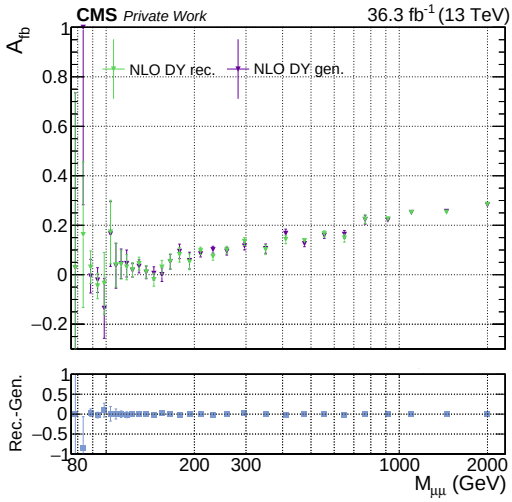

(a) $0 < |y| < 1$

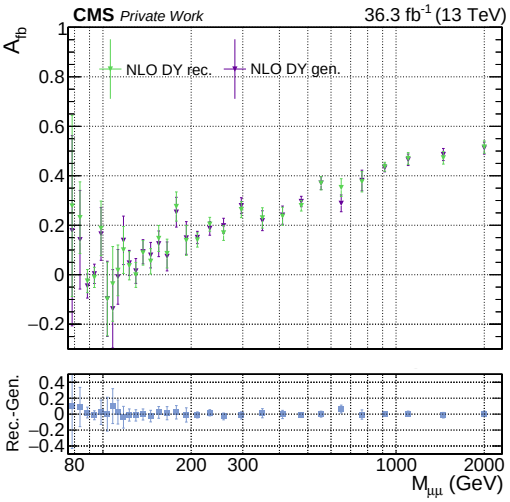

(b) $1 < |y| < 1.25$

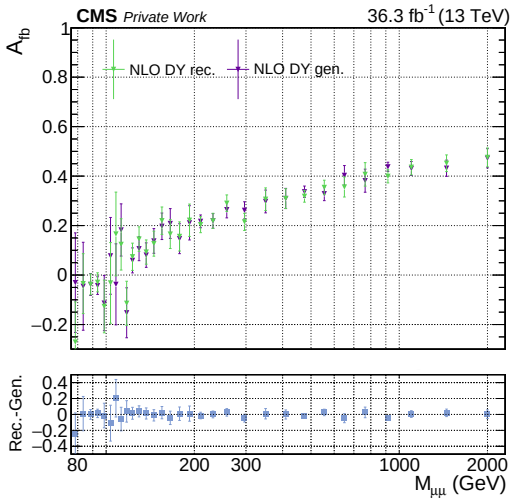

(c) $1.25 < |y| < 1.5$

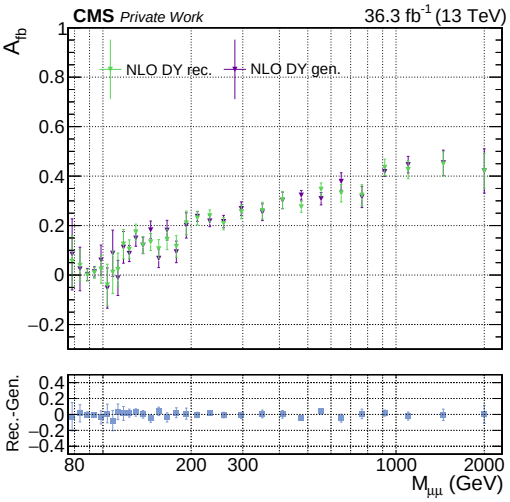

(d) $1.5 < |y| < 2.4$

Figure 10.1: A_{fb} distributions in four ranges of absolute rapidity for the reconstructed NLO Drell–Yan simulation and the NLO Drell–Yan simulation on generator level between 76 GeV and 2000 GeV. The distribution on generator level is shown as a function of $M_{\mu\mu}^{\mathrm{gen.}}$.

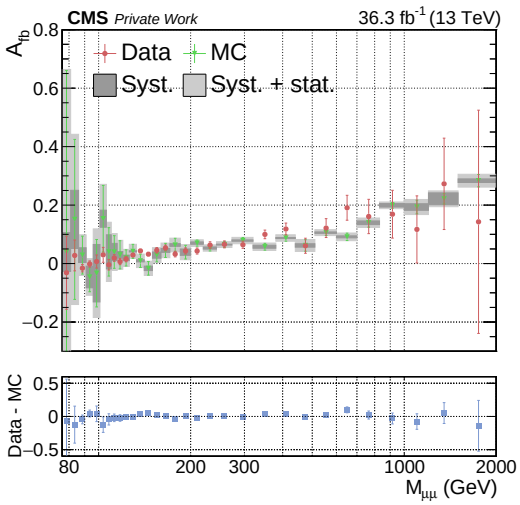

(a) $0 < |y| < 1$

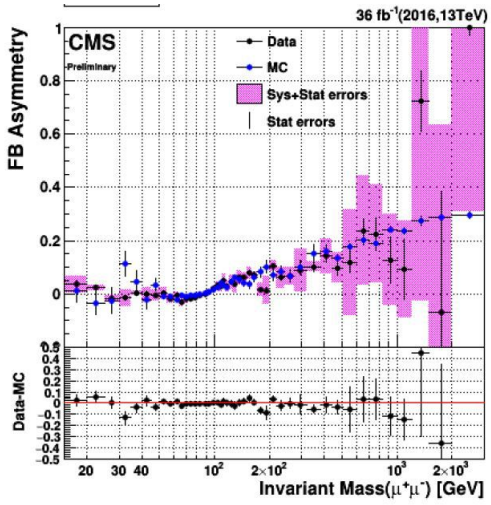

(b) $0 < |y| < 1$

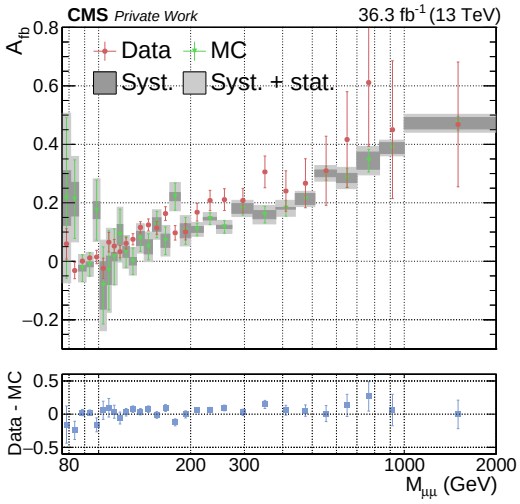

(c) $1 < |y| < 1.25$

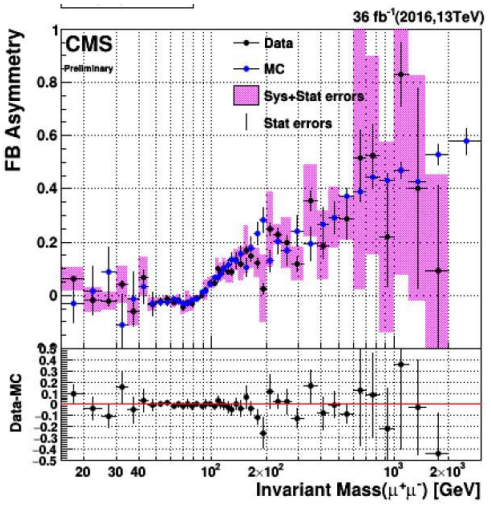

(d) $1 < |y| < 1.25$

Figure 10.2: Comparison between the A_{fb} distributions shown in figure 7.6 and the results obtained in reference [50] for $0 < |y| < 1$ and $1 < |y| < 1.25$. It is important to note that the systematic uncertainties in the right subplots are depicted together with the statistical uncertainties on the data.

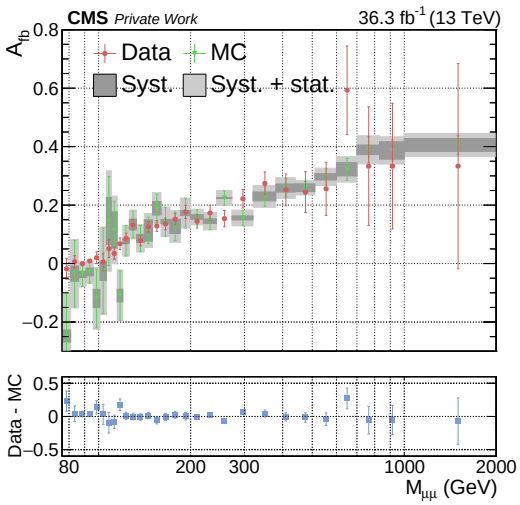

(a) $1.25 < |y| < 1.5$

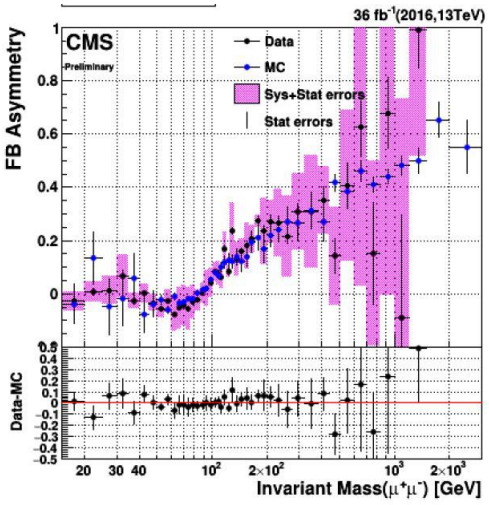

(b) $1.25 < |y| < 1.5$

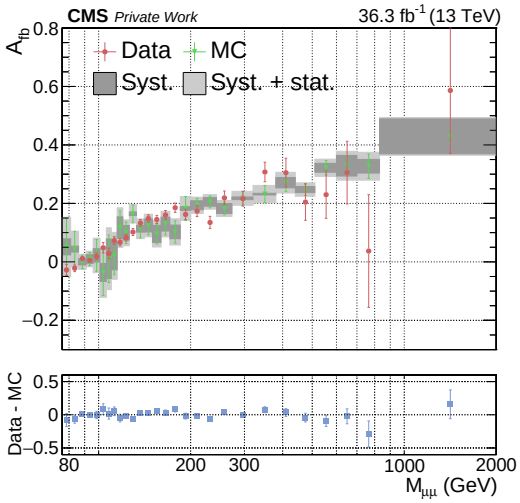

(c) $1.5 < |y| < 2.4$

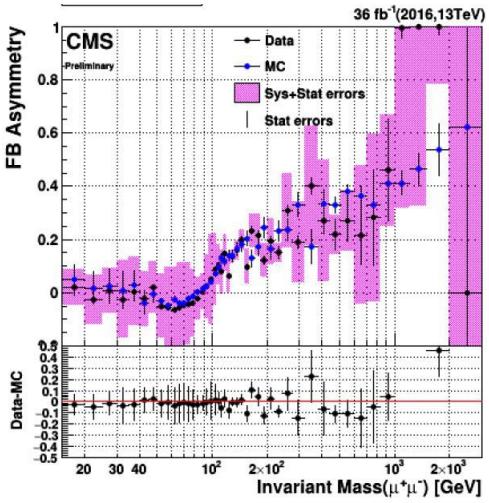

(d) $1.5 < |y| < 2.4$

Figure 10.3: Comparison between the A_{fb} distributions shown in figure 7.6 and the results obtained in reference [50] for $1.25 < |y| < 1.5$ and $1.5 < |y| < 2.4$.

11 References

[1] Max Niedermaier and Martin Reuter. The Asymptotic Safety Scenario in Quantum Gravity. *Living Reviews in Relativity*, 9(1):5, Dec 2006. doi:10.12942/lrr-2006-5.

[2] K. Hagiwara et al. Review of particle properties. *Physical Review D*, 66(1):010001, Jul 2002. doi:10.1103/PhysRevD.66.010001.

[3] M. Danilov at al. Detection of very small neutrino masses in double-beta decay using laser tagging. *Physics Letters B*, 480:12–18, May 2000. doi:10.1016/S0370-2693(00)00404-4.

[4] Gianfranco Bertone and Dan Hooper and Joseph Silk. Particle dark matter: evidence, candidates and constraints. *Physics Reports*, 405(5):279–390, Jan 2005. doi:10.1016/j.physrep.2004.08.031.

[5] P. J. E. Peebles and Bharat Ratra. The cosmological constant and dark energy. *Review of Modern Physics*, 75:559–606, Apr 2003. doi:10.1103/RevModPhys.75.559.

[6] Michael Dine and Alexander Kusenko. Origin of the matter-antimatter asymmetry. *Review of Modern Physics*, 76:1–30, Dec 2003. doi:10.1103/RevModPhys.76.1.

[7] Nima Arkani-Hamed and Savas Dimopoulos and Gia Dvali. The hierarchy problem and new dimensions at a millimeter. *Physics Letters B*, 429:263–272, Jun 1998. doi:10.1016/S0370-2693(98)00466-3.

[8] The LHCb Collaboration. Observation of $J/\psi p$ Resonances Consistent with Pentaquark States in $\Lambda_b^0 \to J/\psi K^- p$ Decays. *Physical Review Letters*, 115:1–72, Aug 2015. doi:10.1103/PhysRevLett.115.072001.

[9] Sidney D. Drell and Tung-Mow Yan. Massive Lepton-Pair Production in Hadron-Hadron Collisions at High Energies. *Physical Review Letters*, 25:316–320, Aug 1970. doi:10.1103/PhysRevLett.25.316.

[10] The CMS Collaboration. Angular coefficients of Z bosons produced in pp collisions at $\sqrt{s} = 8$ TeV and decaying to $\mu^+\mu^-$ as a function of transverse momentum and rapidity. *Physics Letters B*, 750:154–175, 2015. doi:10.1016/j.physletb.2015.08.061.

[11] The CMS Collaboration. Forward-backward asymmetry of Drell-Yan lepton pairs in pp collisions at $\sqrt{s}$=7 TeV. *Physics Letters B*, 718(3):752–772, Jan 2013. doi:10.1016/j.physletb.2012.10.082.

[12] Jonathan L. Rosner. Forward-backward asymmetries in hadronically produced lepton pairs. *Physical Review D*, 54:1078–1082, Jul 1996. doi:10.1103/PhysRevD.54.1078.

[13] Robert Cousins et al. Spin discrimination of new heavy resonances at the LHC. *Journal of High Energy Physics*, 2005(11):046, Nov 2005. `http://stacks.iop.org/1126-6708/2005/i=11/a=046`. [Accessed 12-August-2018].

[14] Jonathan L. Rosner. Off-peak lepton asymmetries from new Z's. *Physical Review D*, 35:2244–2247, Apr 1987. doi:10.1103/PhysRevD.35.2244.

[15] Jonathan L. Rosner. Observability of charge asymmetries for lepton pairs produced in present collider experiments. *Physics Letters B*, 221(1):85–90, Apr 1989. doi:10.1016/0370-2693(89)90197-4.

[16] M. Tanabashi et al. (Particle Data Group), Physcical Review D, (98):030001, 2018. `http://pdg.lbl.gov/2018/reviews/rpp2018-rev-phys-constants.pdf`. [Accessed 26-July-2018].

[17] M. Tanabashi et al. (Particle Data Group), Physcical Review D, (98):030001, 2018. `http://pdg.lbl.gov/2018/tables/rpp2018-sum-gauge-higgs-bosons.pdf`. [Accessed 26-July-2018].

[18] John C. Collins and Davison E. Soper. Angular distribution of dileptons in high-energy hadron collisions. *Physical Review D*, 16:2219–2225, Oct 1977. doi:10.1103/PhysRevD.16.2219.

[19] Nima Arkani-Hamed and Savas Dimopoulos and Gia Dvali. Phenomenology, astrophysics, and cosmology of theories with submillimeter dimensions and TeV scale quantum gravity. *Physical Review D*, 59:086004, Mar 1999. doi:10.1103/PhysRevD.59.086004.

[20] Priscila de Aquino et al. Simulating graviton production at hadron colliders. *Journal of High Energy Physics*, 6:132, Jun 2011. doi:10.1007/JHEP06(2011)132.

[21] JoAnne L. Hewett. Indirect Collider Signals for Extra Dimensions. *Physical Review Letters*, 82:4765–4768, Jun 1999. doi:10.1103/PhysRevLett.82.4765.

[22] CERN. Member states. Jan 2012, `http://cds.cern.ch/record/1997223`. [Accessed 14-July-2018].

[23] CERN Annual reports. Annual Report 2017. CERN in Figures. 2018. `https://e-publishing.cern.ch/index.php/Annual$_$Report/article/view/793`. [Accessed 14-July-2018].

[24] CERN. Accelerators & Schedules. `https://beams.web.cern.ch/content/accelerators-schedules`. [Accessed 14-July-2018].

[25] The CMS Collaboration. Observation of a new boson at a mass of 125 GeV with the CMS experiment at the LHC. *Physics Letters B*, 716(1):30–61, Sep 2012. doi:10.1016/j.physletb.2012.08.021.

[26] CERN. 2017 CERN Electrical Power Consumption. Jan 2018, `http://en.web.cern.ch/sites/en.web.cern.ch/files/ElectricityFlyer2017.pdf`. [Accessed 14-July-2018].

[27] CERN. Experiments. Jul 2012, http://cds.cern.ch/record/1997374. [Accessed 15-July-2018].

[28] The CMS Collaboration. The CMS experiment at the CERN LHC. *Journal of Instrumentation*, 3(08):S08004, Aug 2008. http://stacks.iop.org/1748-0221/3/i=08/a=S08004. [Accessed 12-August-2018].

[29] CMS Luminosity Measurements for the 2016 Data Taking Period. Technical Report CMS-PAS-LUM-17-001, 2017. http://cds.cern.ch/record/2257069. [Accessed 18-July-2018].

[30] The CMS Collaboration. CMS Luminosity Based on Pixel Cluster Counting - Summer 2013 Update. 2013. https://cds.cern.ch/record/1598864/?ln=de. [Accessed 18-July-2018].

[31] Simone Alioli et al. A general framework for implementing NLO calculations in shower Monte Carlo programs: the POWHEG BOX. *Journal of High Energy Physics*, 6:43, Jun 2010. doi:10.1007/JHEP06(2010)043.

[32] Torbjörn Sjöstrand et al. An introduction to PYTHIA 8.2. *Computer Physics Communications*, 191:159–177, 2015. doi:10.1016/j.cpc.2015.01.024.

[33] Richard D. Ball et al. Parton distributions for the LHC run II. *Journal of High Energy Physics*, 4:40, Apr 2015. doi:10.1007/JHEP04(2015)040.

[34] Ye Li and Frank Petriello. Combining QCD and electroweak corrections to dilepton production in the framework of the FEWZ simulation code. *Physical Review D*, 86:094034, Nov 2012. doi:10.1103/PhysRevD.86.094034.

[35] Ryan Gavin and Ye Li and Frank Petriello and Seth Quackenbush. FEWZ 2.0: A code for hadronic Z production at next-to-next-to-leading order. *Computer Physics Communications*, 182(11):2388 – 2403, 2011. doi:10.1016/j.cpc.2011.06.008.

[36] Markus Radziej. Private communication, Jul 2018.

[37] Michal Czakon and Alexander Mitov. Top++: A program for the calculation of the top-pair cross-section at hadron colliders. *Computer Physics Communications*, 185(11):2930 – 2938, 2014. doi:10.1016/j.cpc.2014.06.021.

[38] Johan Alwall et al. Madgraph 5: going beyond. *Journal of High Energy Physics*, 6:128, Jun 2011. doi:10.1007/JHEP06(2011)128.

[39] Thomas Binoth and Mariano Ciccolini and Nikolas Kauer and Michael Krämer. Gluon-induced W -boson pair production at the LHC. *Journal of High Energy Physics*, 12:046, 2006. http://stacks.iop.org/1126-6708/2006/i=12/a=046. [Accessed 18-July-2018].

[40] John M. Campbell and R.K. Ellis. MCFM for the Tevatron and the LHC. *Nuclear Physics B - Proceedings Supplements*, 205-206:10–15, 2010. doi:10.1016/j.nuclphysbps.2010.08.011.

[41] CERN Physics Validation Group. Utilities for Accessing Pileup Information for Data, 2012. `https://twiki.cern.ch/twiki/bin/viewauth/CMS/PileupJSONFileforData`.

[42] The CMS Collaboration. Performance of the CMS muon detector and muon reconstruction with proton-proton collisions at $\sqrt{s} = 13$ TeV. *Journal of Instrumentation*, 13:6–15, Apr 2018. doi:10.1088/1748-0221/13/06/P06015.

[43] The CMS Collaboration and the LHCb Collboration. Observation of the rare ${B_S}^0 \to \mu^+\mu^-$ decay from the combined analysis of CMS and LHCb data. *Nature*, 522:68–72, Jun 2015. doi:10.1088/1748-0221/13/06/P06015.

[44] Rudolf Fruehwirth. Application of Kalman filtering to track and vertex fitting. *Nuclear Instruments and Methods in Physics A*, 262(2-3):444–450, Dec 1987. doi:10.1016/0168-9002(87)90887-4.

[45] The CMS Collaboration. Search for High-Mass Resonances Decaying to Muon Pairs in pp Collisions at $\sqrt{s} = 13$ TeV with the full 2016 data set of 37 fb and combination with 2015 result. 2016. `http://cms.cern.ch/iCMS/jsp/db_notes/3135noteInfo.jsp?cmsnoteid=CMS%5C%20AN-2016/391`. [Accessed 03-August-2018].

[46] Jon Butterworth et al. PDF4LHC recommendations for LHC Run II. *Journal of Physics G: Nuclear and Particle Physics*, 43(2):023001, 2016. doi:10.1088/0954-3899/43/2/023001.

[47] The CMS Collaboration. Search for high-mass resonances in dilepton final states in proton-proton collisions at $\sqrt{s}$=13 TeV. *Journal of High Energy Physics*, 06(120), 2018. doi:10.1007/JHEP06(2018)120.

[48] The CMS Collaboration. Forward-backward asymmetry of Drell-Yan lepton pairs in pp collisions at $\sqrt{s} = 8$ TeV. *European Physics Journal C*, 76, Jun 2016. doi:10.1140/epjc/s10052-016-4156-z.

[49] The CMS Collaboration. Search for high-mass resonances in dilepton final states in proton-proton collisions at $\sqrt{s} = 13$ TeV. *Journal of High Energy Physics*, 06:120, Jul 2018. doi:10.1007/JHEP06(2018)120.

[50] The CMS Collaboration. Forward-backward Asymmetry of Drell-Yan Muon Pairs in pp collisions at 13 TeV. 2018. `http://cms.cern.ch/iCMS/user/noteinfo?cmsnoteid=CMS%20AN-2017/155`. [Accessed 22-August-2018].